

Geometric Decomposition of Statistical Inference through Gradient Flow and Co-Monotonicity Measures*

Pawel Gajer^{1†} and Jacques Ravel¹

¹University of Maryland School of Medicine

Abstract

Understanding feature-outcome associations in high-dimensional data remains challenging when relationships vary across subpopulations, yet standard methods assuming global associations miss context-dependent patterns, reducing statistical power and interpretability. We develop a geometric decomposition framework offering two strategies for partitioning inference problems into regional analyses on data-derived Riemannian graphs. Gradient flow decomposition uses path-monotonicity-validated discrete Morse theory to partition samples into basins where outcomes exhibit monotonic behavior. Co-monotonicity decomposition leverages association structure: vertex-level coefficients measuring directional concordance between outcome and features, or between feature pairs, define embeddings of samples into association space. These embeddings induce Riemannian k-NN graphs on which bi-clustering identifies co-monotonicity cells (coherent regions) and feature modules. This extends naturally to multi-modal integration across multiple feature sets. Both strategies apply independently or jointly, with Bayesian posterior sampling providing credible intervals.

Keywords: geometric data analysis, gradient flow, co-monotonicity, Riemannian graphs, statistical inference, high-dimensional data, manifold learning, graph Laplacian, multiple testing, microbiome analysis

*Research reported in this publication was supported by grant number INV-048956 from the Gates Foundation.

†Corresponding author: pgajer@gmail.com

Software: The methods are implemented in the R package `gflow`, available at <https://github.com/pgajer/gflow>.

1. Introduction

Understanding which features associate with outcomes in high-dimensional data remains one of the central challenges in modern statistical analysis. Consider a microbiome study investigating spontaneous preterm birth [14, 11], where researchers measure hundreds of bacterial taxa across hundreds of samples. A particular phylotype might promote disease risk in women with one microbial community composition while showing no effect or even protective association in women with different community structures. Yet traditional correlation and regression methods that assume global, homogeneous relationships across all samples will average over these conflicting signals, potentially concluding that no association exists when in fact multiple distinct context-dependent mechanisms operate simultaneously.

This phenomenon of spatially heterogeneous associations appears throughout high-dimensional biomarker studies. In single-cell genomics, gene expression programs exhibit cell-type-specific relationships with outcomes [28]. In spatial transcriptomics, tissue architecture creates regions where the same molecular features play different functional roles [4]. In ecological data, species interactions vary across environmental gradients [19]. The common thread is that the ambient high-dimensional feature space contains subpopulations or regions where statistical relationships differ fundamentally, yet these regions are unknown a priori and must be discovered from data. When associations of opposite sign cancel in global analyses, investigators miss biologically meaningful mechanisms entirely, and the resulting models provide no basis for stratified interventions or personalized predictions.

What is needed, then, is a framework that naturally discovers the contextual structure latent in high-dimensional data and partitions the sample space into regions of homogeneous associative behavior. The partition itself should emerge from geometric properties of the data, which encode the complex interactions between features implicit in the ambient representation, rather than being imposed through arbitrary choices. By deconvoluting these hidden association patterns and making them explicit through geometric decomposition, the framework enables rigorous uncertainty quantification that respects both the spatial dependencies in graph-structured data and the exploratory nature of discovering structure and testing associations simultaneously.

A fundamental characteristic of high-dimensional data poses both challenge and opportunity: while datasets may contain hundreds or thousands of measured features, the underlying system often operates through far fewer degrees of freedom. Genomic studies measure tens of thousands of genes, yet cellular states often organize along a small number of developmental or functional axes [29]. Microbiome samples with hundreds of bacterial taxa concentrate near community type structures rather than filling the ambient space [22, 1]. Social network data with extensive demographic and behavioral variables frequently reduces to a handful of latent factors [17]. The manifold hypothesis [26, 13] formalizes this observation: high-dimensional data typically concentrates near low-dimensional manifolds embedded in the ambient feature space. While real data rarely forms smooth manifolds (exhibiting noise, stratification, and singular structures) the core insight remains valid that intrinsic dimensionality is far lower than nominal dimensionality, and that this geometric structure can be exploited for inference.

Geometric data analysis adopts a coordinate-free perspective, representing data through graphs or simplicial complexes that capture intrinsic relationships between samples. Rather than computing $E[Y|X]$ where $X \in \mathbb{R}^p$, we shift to computing $E[Y|G(X, y)]$ where $G(X, y)$ denotes a density-aware graph constructed from the predictor matrix X and observed response y . This reformulation makes the geometric structure explicit: statistical inference operates directly on the graph that encodes how samples relate to one another.

We work specifically with Riemannian graphs that possess rich local metric structure beyond simple edge weights. These graphs arise naturally from intersection k-nearest neighbor constructions interpreted through nerve complexes. Each vertex v corresponds to a sample, and the vertex mass $m_0(v)$ reflects the local density of samples in that region. Edges connect nearby samples, with edge masses $m_1(e)$ capturing the geometric extent of neighborhoods that share the edge. The Riemannian structure on the graph is encoded by the vertex mass matrix M_0 (diagonal, with entries $m_0(v)$) and the edge inner product matrix M_1 . While M_0 is determined by vertex masses alone, M_1 encodes more complex geometric relationships: beyond edge masses, it captures angular information between incident edges through inner products computed from the symmetrized graph Laplacian, defining a complete inner product structure on the space of edge chains [15]. The normalized graph Laplacian $L_{\text{norm}} = M_0^{-1/2} L_0 M_0^{-1/2}$, constructed from these masses, governs diffusion processes on the graph [8] and enables spectral filtering methods for signal recovery [25, 2].

Our approach builds fundamentally on Morse-Smale regression, introduced by Gerber et al. [16]. Their pioneering work brought ideas from Morse theory in differential topology [21, 30] into the statistical inference context, using gradient flow analysis to partition the feature space into cells determined by pairs of local extrema of the conditional expectation surface, then performing separate regression analyses within each cell. The framework elegantly connects differential topology with statistical practice, providing interpretable regional decompositions that respect the geometry of the prediction landscape. However, translating this continuous theory to the discrete, noisy setting of finite sample data presents several fundamental challenges. First, robust estimation of conditional expectations on graphs constructed from finite samples remains difficult. Moreover, even if the conditional expectation estimate were a smooth function, sampling it on a finite point set inevitably introduces spurious local extrema that do not correspond to genuine features of the underlying continuous function. Without methods to distinguish signal from noise in the extrema structure, the resulting cell decomposition may fragment the space unnecessarily or preserve spurious features. Second, real data-derived graphs typically contain long edges that connect distant points, creating basin jumping artifacts where gradient trajectories incorrectly cross between basins by following a single long edge rather than a path through intermediate samples.

Third, applying standard linear models within each gradient flow cell assumes that local linearity captures associations once heterogeneity is resolved through decomposition. However, even if relationships within cells are indeed locally linear, high-dimensional feature sets typically exhibit strong multicollinearity, with many features highly correlated with each other. Lasso-type regularization [27] can partially address this through automated feature selection, but different lasso variants handle correlated features in problematic ways: standard lasso tends to arbitrarily select one representative from a group of correlated features, while elastic net [31] includes entire groups but with potentially excessive shrink-

age. Moreover, if investigators wish to model how features interact with each other to influence outcomes, interaction terms must be pre-specified and included in the regression. With hundreds or thousands of features, the combinatorial explosion of potential interactions becomes computationally intractable and statistically underpowered [3, 12]. These challenges of multicollinearity, arbitrary feature selection, and unmodeled interactions suggest that alternative approaches to quantifying associations within cells may prove more robust than fitting linear models. Finally, the discrete-to-discrete translation requires careful treatment of the graph structure itself: working with mutual k-nearest neighbor graphs with simple edge weights may not capture the richer geometric structure that density-aware Riemannian metrics provide.

Our approach addresses these challenges while extending the Morse-Smale framework in two fundamental directions. Unlike variable selection or dimension reduction approaches that retain all samples while modifying the feature representation [27, 12, 26, 23], geometric decomposition stratifies the sample space itself into regions where different features may be relevant or where the same features operate through different mechanisms.

Figures 1 and 2 illustrate these concepts. Figure 1 demonstrates gradient-flow decomposition in one dimension, showing how a function with multiple local extrema naturally partitions into regions with homogeneous statistical behavior. Critical points (local minima and maxima) form boundaries defining ascending and descending basins, whose intersections create gradient-flow cells with monotonic behavior.

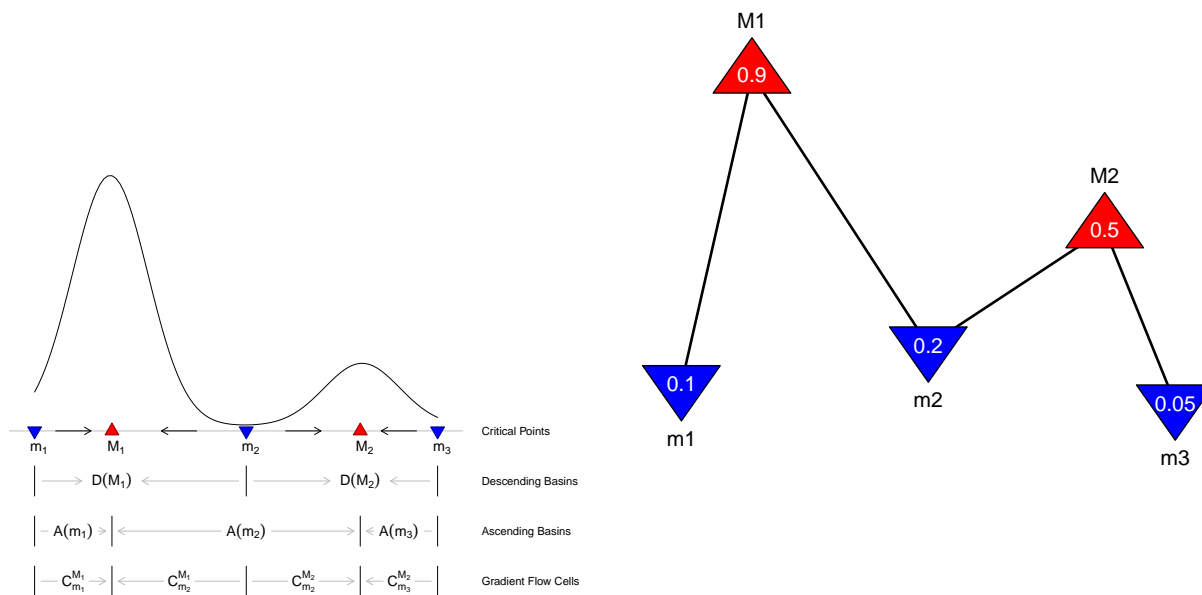


Figure 1: Domain decomposition via gradient flow. Panel A: One-dimensional function with local minima (m_1, m_2, m_3) and maxima (M_1, M_2), showing gradient directions and partitioning into ascending/descending basins and gradient flow cells. Panel B: Gradient flow graph with vertices as critical points (labeled with function values) and edges connecting minimum-maximum pairs, enabling monotonic statistical modeling within each cell.

The gradient flow graph serves as a one-dimensional skeleton capturing the essential shape of the prediction landscape, with edges representing natural non-linear generalizations of

principal directions in classical statistical methods. Figure 2 extends this framework to two dimensions, revealing additional complexities: non-trivial cell boundaries with irregular geometries, meaningful transition regions through saddle points, and the challenge of distinguishing statistically significant features from spurious patterns arising from finite sampling.

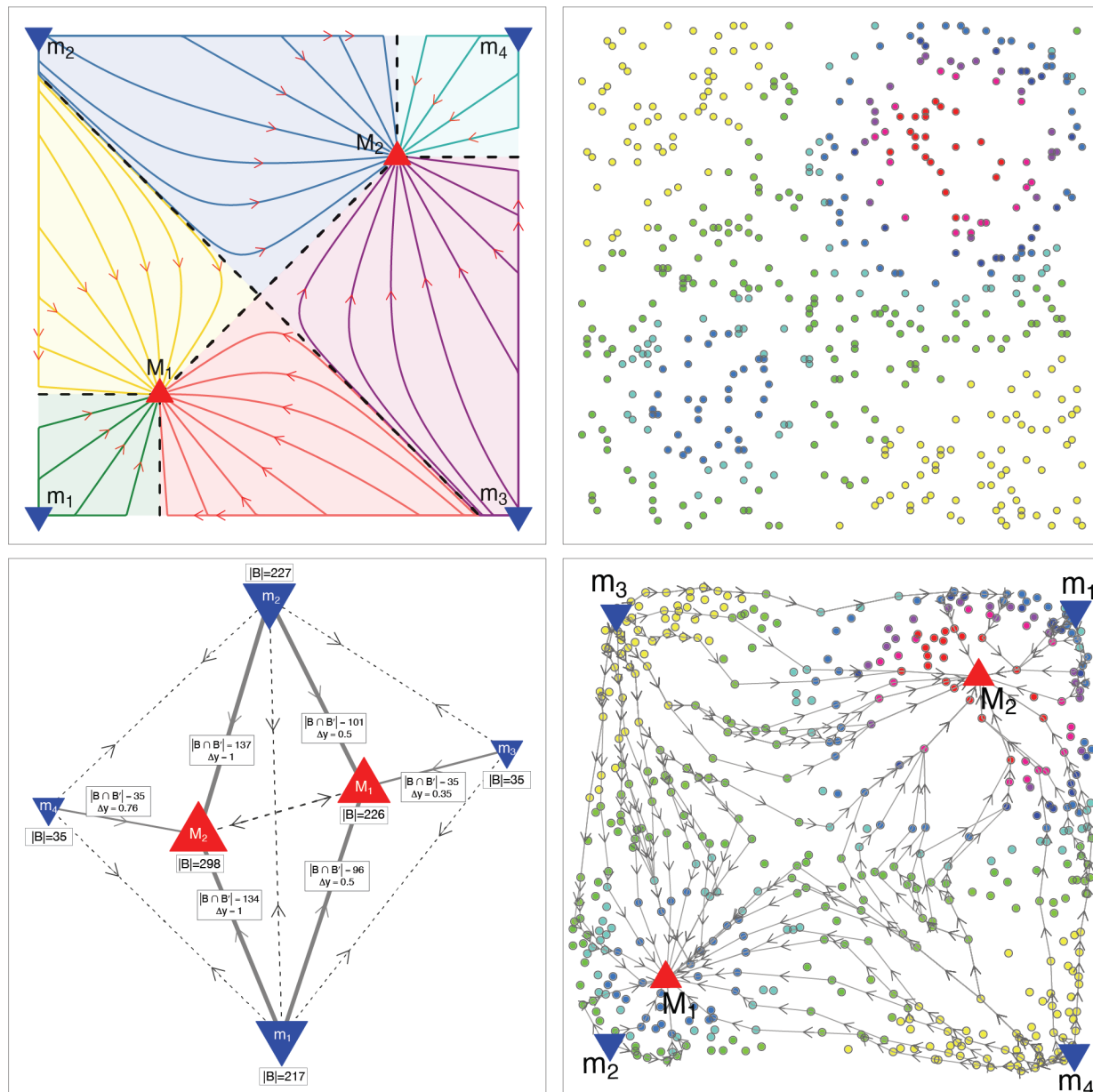


Figure 2: Gradient flow decomposition of a two-Gaussian mixture on $[0, 1]^2$. Top-left: Continuous function with critical points, gradient trajectories, and cell boundaries. Top-right: Random sample with color-coded function values. Bottom-right: k -nearest neighbor graph ($k = 36$) with selected gradient trajectories. Bottom-left: Gradient flow complex where solid edges connect minimum-maximum pairs and dashed edges represent minimum-minimum cells with saddle points; edges shown for cells with at least 25 points.

The first strategy employs gradient flow analysis to partition samples based on the geom-

etry of the outcome surface. Given a smoothed estimate $\hat{y} : V \rightarrow \mathbb{R}$ of the conditional expectation on graph vertices, we construct the discrete gradient flow by iteratively moving from each vertex toward neighbors with increasing (for ascending flow) or decreasing (for descending flow) function values. The trajectories of these flows partition vertices into basins of attraction: all vertices whose ascending flows terminate at the same local minimum belong to that minimum’s ascending basin, and similarly for descending flows toward local maxima. The intersections of ascending and descending basins define gradient flow cells $C(m, M) = B(m) \cap B(M)$ where the outcome function exhibits monotonic behavior. This construction realizes a discrete Morse-Smale complex on the graph, partitioning the sample space into regions where the outcome surface has uniform qualitative structure. We address the long edge problem through path monotonicity validation: for edges connecting distant points, we verify that the outcome function remains monotonic along the shortest alternative path. Only edges passing this validation participate in gradient flow computation, preventing basin jumping artifacts.

The second strategy emerged from considering how to quantify feature associations within gradient flow cells. Since the smoothed outcome \hat{y} exhibits monotonic behavior along gradient trajectories within each cell, a natural approach to identifying associated features would measure their monotonicity along these same trajectories. This path-based perspective, treating monotonicity as a functor of paths and individual functions, suggested an immediate generalization: rather than measuring single-function monotonicity along paths, we could measure co-monotonicity between pairs of functions, quantifying whether they vary together or oppositely along edges. A further abstraction yields vertex-level measures by aggregating edge-wise co-monotonicity over neighborhoods, producing coefficients that capture directional concordance locally while being independent of any particular path structure.

Co-monotonicity coefficients measure directional concordance between functions at individual graph vertices: for functions $y, z : V \rightarrow \mathbb{R}$, the coefficient at vertex v quantifies whether y and z tend to change together (positive co-monotonicity), opposite (negative), or independently (near zero) across edges incident to v . By computing co-monotonicity between an outcome y and features in a set $Z = \{z_1, \dots, z_m\}$, as well as between feature pairs, we obtain association profiles for each sample. Figure 3 illustrates these profiles in a microbiome application, where hierarchical clustering reveals coherent blocks of samples with similar association patterns and features with coordinated outcome relationships. These profiles define embeddings into association space, on which we construct k-nearest neighbor graphs and apply spectral biclustering [9, 18] to identify co-monotonicity cells—vertex regions and feature modules exhibiting coherent multivariate association patterns. Where gradient flow partitions based on how outcomes vary spatially, co-monotonicity partitioning discovers regions based on which features associate with outcomes and how features relate to each other. The framework extends naturally to multi-modal data integration, computing association matrices across feature sets and their cross-associations to construct embeddings that integrate information across modalities.

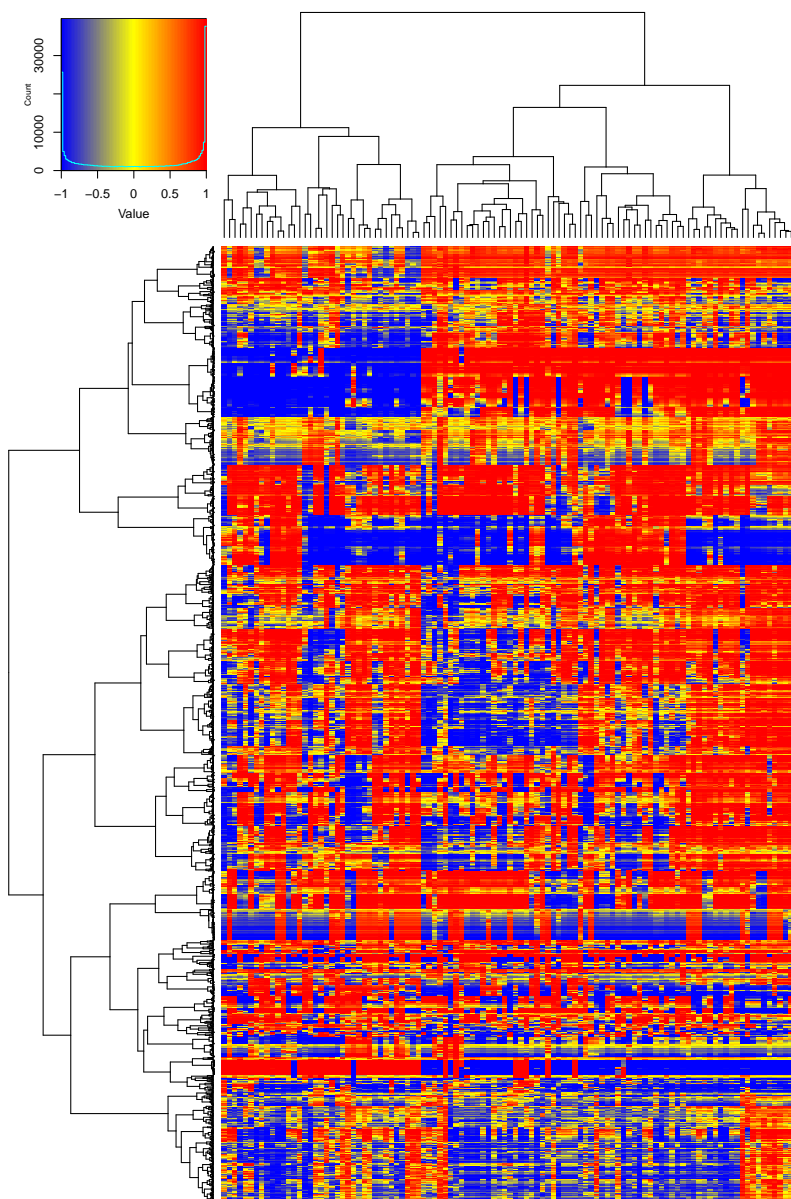


Figure 3: Co-monotonicity association profiles in vaginal microbiome data. Heatmap shows vertex-level co-monotonicity coefficients between spontaneous preterm birth outcome and bacterial phylotype abundances across samples from pregnant women (rows: samples, columns: phylotypes). Hierarchical clustering on both axes reveals coherent blocks: samples (rows) group by shared association patterns, while phylotypes (columns) cluster by co-varying relationships with the outcome. Red indicates positive co-monotonicity (phylotype and outcome increase together), blue indicates negative co-monotonicity (inverse relationship), and yellow indicates independence. The block structure demonstrates how biclustering on these association profiles identifies co-monotonicity cells—regions where specific feature modules exhibit consistent outcome associations.

The two strategies can be applied independently or jointly. Independent application suits exploratory analysis discovering structure from one perspective. Joint application enables assessment of concordance: do outcome-driven gradient flow cells align with association-

driven co-monotonicity cells? High concordance suggests that regions of similar outcome values arise from consistent underlying mechanisms, while discordance indicates that similar outcomes can emerge through different pathways.

Our work extends Morse-Smale regression [16] through robust conditional expectation estimation on density-aware Riemannian graphs, systematic treatment of spurious extrema through prominence filtering and basin overlap clustering, path monotonicity validation to resolve long edge artifacts, and co-monotonicity measures as alternatives to linear models within cells. Beyond these technical advances, our introduction of association-based decomposition through co-monotonicity complements Gerber’s outcome-based approach, providing a second lens for discovering structure.

The framework situates naturally within geometric data analysis rather than topological data analysis. While TDA [5, 10] emphasizes topological invariants like homology groups and persistence diagrams that remain unchanged under continuous deformations, GDA focuses on geometric properties like distances, angles, curvature, and geodesics that depend on the specific metric structure. Our Riemannian graphs with their vertex and edge masses capture local geometry that spectral methods can exploit for inference. The gradient flow we compute respects this geometry through derivative weighting in co-monotonicity coefficients and through the Riemannian metric implicit in the normalized Laplacian. This geometric emphasis connects our work more closely to manifold learning [26, 23, 8] and spectral graph theory [6, 20] than to persistent homology, though we acknowledge that the basin complex structure we compute has topological aspects.

From a statistical perspective, our geometric decomposition provides data-driven stratification for inference. Stratified sampling and stratified testing are well-established ideas in statistics [7], typically requiring investigators to specify strata based on known covariates. Our contribution is making stratification itself a geometric inference problem: the strata emerge from graph structure through gradient flow or co-monotonicity analysis rather than being predetermined. This connects to recent work on conditional independence testing [24] and context-specific associations, but grounds these ideas in explicit geometric partitions of the sample space.

The Bayesian inference framework we develop through posterior sampling on weighted Laplacians provides credible intervals that respect the geometry of the data manifold while enabling principled multiple testing corrections through the geometric structure of co-monotonicity cells.

Section 2 establishes the mathematical framework of Riemannian graphs, functions on graphs, and discrete gradient flow. Section 3 addresses the long edge problem through path monotonicity validation and presents basin computation algorithms. Section 4 introduces co-monotonicity coefficients, derives their properties, and develops matrix extensions for multivariate analysis. Section 5 establishes statistical inference procedures including vertex-wise permutation testing and Bayesian credible intervals via posterior sampling. Section 6 presents the geometric multiple testing framework through co-monotonicity cells and biclustering. Section 7 discusses computational implementation in the gflow R package. Section 8 concludes with discussion of limitations, relationships to other methods, and future directions.

2. Mathematical Framework: Riemannian Graphs and Discrete Gradient Flow

We begin with a question that motivates the entire geometric framework: given observations x_1, \dots, x_n in \mathbb{R}^d with associated outcomes y_1, \dots, y_n , how should we represent the inherent structure of the data in a way that enables both robust estimation of conditional expectations and natural stratification of the sample space? Standard approaches treat the data as points in Euclidean space, but this perspective obscures the crucial geometric relationships that determine how information should propagate between observations during inference.

2.1 From Point Clouds to Weighted Graphs

Consider a simple example. Suppose we observe ten points arranged in two clusters in the plane, with five points concentrated near $(0, 0)$ and five near $(1, 1)$. Traditional kernel methods place a Gaussian at each point and sum, yielding a smooth density estimate. Yet this approach treats all pairwise distances identically and fails to recognize that points within clusters share local geometry while points in different clusters do not, despite having similar distances to cluster boundaries.

The k -nearest neighbor graph provides a more geometric perspective. We connect each point to its k nearest neighbors, creating a graph $G = (V, E)$ where vertices correspond to observations and edges encode proximity relationships. For our two-cluster example with $k = 4$, edges connect points within each cluster but not across clusters (assuming sufficient separation). The graph structure reveals the discrete geometry: the two clusters appear as connected components, and any function defined on vertices can diffuse within components but not between them.

However, unweighted graphs lose important information. In regions where points lie densely, small Euclidean distances separate neighbors, while in sparse regions, large distances occur. A single long edge might connect distant points that happen to be mutual nearest neighbors, creating an artificial bridge that permits gradient flow to jump between geometrically distant regions. We require vertex and edge weights that encode both local density and geometric scale.

2.2 Riemannian Structure Through Mass Assignment

We construct a Riemannian graph through systematic assignment of masses to vertices and edges. The vertex mass $m_0(v)$ at vertex v quantifies the local concentration of observations, while edge masses $m_1(e)$ measure geometric relationships between neighborhoods. These masses induce a complete metric structure on the graph, enabling precise measurement of distances, angles, and volumes.

Let $N_k(x_i)$ denote the closed k -nearest neighbor ball of observation x_i , and let $\mathcal{U} = \{N_k(x_1), \dots, N_k(x_n)\}$ be the covering of the dataset by these neighborhoods. The nerve

complex of this covering has vertices corresponding to observations, with simplices recording multi-way neighborhood intersections. We focus on the 1-skeleton (vertices and edges), which forms a graph where an edge $[i, j]$ exists whenever $N_k(x_i) \cap N_k(x_j) \neq \emptyset$.

Definition 1 (Vertex Mass). The vertex mass $m_0(i)$ represents the measure of the neighborhood $N_k(x_i)$. In practice, we use density-surrogate weights

$$m_0(i) = w(x_i) = (\varepsilon + d_k(x_i))^{-\alpha} \quad (1)$$

where $d_k(x_i)$ denotes the distance from x_i to its k -th nearest neighbor, $\varepsilon > 0$ is a small regularization constant, and $\alpha \in [1, 2]$ controls the degree of density weighting. The vertex masses are normalized so that $\sum_{i=1}^n m_0(i) = n$.

The formula inverts neighborhood radius: points in dense regions have small d_k and receive large mass, while isolated points have large d_k and receive small mass. The exponent α modulates sensitivity to density variation. Alternative formulations using exponential or rational kernels provide smooth density dependence.

Definition 2 (Edge Mass and Inner Products). For an edge $e = [i, j]$, the edge mass $m_1(e)$ equals the total vertex mass in the neighborhood intersection:

$$m_1([i, j]) = \sum_{\ell: x_\ell \in N_k(x_i) \cap N_k(x_j)} m_0(\ell). \quad (2)$$

More generally, for two edges $e_{ij} = [i, j]$ and $e_{is} = [i, s]$ sharing vertex i , their inner product equals the triple intersection mass:

$$\langle e_{ij}, e_{is} \rangle = \sum_{\ell: x_\ell \in N_k(x_i) \cap N_k(x_j) \cap N_k(x_s)} m_0(\ell). \quad (3)$$

These inner products encode geometric relationships beyond simple edge weights. Two edges sharing a vertex are orthogonal if their corresponding neighborhoods intersect only at their common vertex, while edges with large triple intersection mass form acute angles. The collection of all edge inner products assembles into the edge mass matrix M_1 , with diagonal entries $M_1(e, e) = m_1(e)$ and off-diagonal entries $M_1(e_{ij}, e_{is}) = \langle e_{ij}, e_{is} \rangle$.

We encode the vertex masses in a diagonal matrix $M_0 = \text{diag}(m_0(1), \dots, m_0(n))$. The pair (M_0, M_1) constitutes the Riemannian structure, determining inner products on the spaces of vertex chains C_0 and edge chains C_1 .

2.3 The Graph Laplacian and Diffusion

The Riemannian structure induces differential operators through the Hodge decomposition. We begin with the boundary operator $B_1 : C_1 \rightarrow C_0$, which maps edge chains to vertex chains according to

$$(B_1\alpha)(i) = \sum_{j \in N(i)} (\alpha([j, i]) - \alpha([i, j])), \quad (4)$$

where $N(i)$ denotes the neighborhood of vertex i and $[i, j]$ denotes the oriented edge from i to j . The adjoint operator $B_1^* : C_0 \rightarrow C_1$ with respect to the inner products defined by M_0 and M_1 satisfies

$$\langle B_1 \alpha, f \rangle_{M_0} = \langle \alpha, B_1^* f \rangle_{M_1} \quad (5)$$

for all edge chains α and vertex chains f . This determines

$$B_1^* = M_1^{-1} B_1^T M_0. \quad (6)$$

Definition 3 (Hodge Laplacian). The Hodge Laplacian on vertex chains (the graph Laplacian) is defined as

$$L_0 = B_1^* B_1 = M_0^{-1} B_1^T M_1^{-1} B_1. \quad (7)$$

This operator governs diffusion on the weighted graph. For computational purposes, we work with the symmetrized normalized Laplacian

$$L_{\text{norm}} = M_0^{-1/2} L_0 M_0^{-1/2} = M_0^{-1/2} B_1^T M_1^{-1} B_1 M_0^{-1/2}, \quad (8)$$

which has eigenvalues in $[0, 2]$ and admits spectral decomposition through standard symmetric eigensolvers.

The heat equation $\partial \rho / \partial t = -L_0 \rho$ describes how vertex masses evolve under diffusion. The solution $\rho(t) = \exp(-tL_0)\rho(0)$ applies the heat kernel to the initial distribution. For small t , diffusion smooths local irregularities while preserving global structure; for large t , all mass flows toward the stationary distribution. The Riemannian structure determines diffusion rates: edges with large mass (small Riemannian length) facilitate rapid exchange, while edges with small mass (large Riemannian length) impede flow.

2.4 Functions on Graphs and the Discrete Gradient

We consider real-valued functions $f : V \rightarrow \mathbb{R}$ defined on graph vertices. Such functions represent observed outcomes, fitted predictions, or any other vertex-associated quantities. The gradient of f measures how the function changes across edges.

Definition 4 (Discrete Gradient). For a function $f : V \rightarrow \mathbb{R}$, the gradient is the linear operator $\nabla f : E \rightarrow \mathbb{R}$ defined on oriented edges. For an edge $e = [i, j]$ directed from vertex i to vertex j , we define

$$(\nabla f)(e) = \frac{m_0(j)f(j) - m_0(i)f(i)}{m_1(e)}, \quad (9)$$

where the vertex masses in the numerator weight the function values according to local density, and the edge mass in the denominator normalizes by the geometric scale of the neighborhood intersection.

This formula has intuitive interpretation. In regions where both vertices have equal mass (uniform density), the gradient reduces to the function difference divided by edge mass, analogous to a directional derivative where edge mass acts as effective distance. In non-uniform regions, vertices with larger mass contribute more strongly, reflecting that these

vertices represent denser neighborhoods where the function value has greater statistical weight.

The gradient satisfies a fundamental variational property. Among all edge-valued functions ϕ with specified values at vertices, the gradient minimizes the energy

$$\mathcal{E}(\phi) = \sum_{e \in E} m_1(e) |\phi(e)|^2, \quad (10)$$

subject to the boundary constraint $(B_1\phi)(i) = \sum_{j \in N(i)} m_0(j) (\phi([i, j]) - \phi([j, i])) = 0$ for all interior vertices. This characterizes the gradient as the minimizer of weighted squared variation, balancing smoothness against fidelity to vertex values.

2.5 Critical Points and the Discrete Morse Complex

A vertex v is a local extremum if the function increases or decreases strictly when moving to any neighbor. Formally, v is a local minimum if $f(v) < f(u)$ for all $u \in N(v)$, and a local maximum if $f(v) > f(u)$ for all $u \in N(v)$. These definitions extend classical Morse theory to the discrete setting.

Definition 5 (Critical Points). The set of critical points consists of all local minima, local maxima, and (in certain formulations) saddle points where the Hessian has both positive and negative eigenvalues. For functions on graphs, we identify local extrema directly from the vertex function values through neighborhood comparisons.

Critical points organize the qualitative structure of the function. Between any local minimum m and local maximum M , there exists a connecting path along which the function increases monotonically. These monotone paths define the gradient flow structure.

Definition 6 (Gradient Flow Trajectories). Starting from a vertex v , the ascending gradient trajectory follows edges of steepest ascent: at each step, we move to the neighbor u with maximal function value $f(u) > f(v)$, continuing until reaching a local maximum where no higher neighbor exists. Similarly, the descending trajectory follows steepest descent to a local minimum.

We denote the terminus of the ascending trajectory from v as $\pi_{\uparrow}(v)$, and the terminus of the descending trajectory as $\pi_{\downarrow}(v)$. These maps partition the vertex set into basins of attraction.

Definition 7 (Basins of Attraction). For a local minimum m , the ascending basin is

$$A(m) = \{v \in V : \pi_{\uparrow}(v) = m\}, \quad (11)$$

containing all vertices whose ascending flow terminates at m . For a local maximum M , the descending basin is

$$D(M) = \{v \in V : \pi_{\downarrow}(v) = M\}, \quad (12)$$

containing all vertices whose descending flow terminates at M .

The basins satisfy $\bigcup_m A(m) = V$ and $\bigcup_M D(M) = V$, providing complete partitions of the vertex set. The intersections $C(m, M) = A(m) \cap D(M)$ define gradient flow cells, which are regions where both ascending and descending flows have unique termini.

Theorem 8 (Monotonicity in Gradient Flow Cells). *Within a gradient flow cell $C(m, M)$, the function f is monotone along all paths connecting the minimum m to the maximum M . Specifically, any path $m = v_0, v_1, \dots, v_k = M$ contained in $C(m, M)$ satisfies $f(v_0) < f(v_1) < \dots < f(v_k)$.*

The theorem follows from the definitions: within $C(m, M)$, ascending flow from any vertex moves toward M , so function values increase along ascending paths; descending flow moves toward m , so function values decrease along descending paths. Any monotone path from m to M must ascend throughout, ensuring strict increase.

This monotonicity property provides the foundation for regional inference. Within each cell, the outcome exhibits uniform qualitative behavior (monotone increase from minimum to maximum), suggesting that feature associations should also exhibit spatial homogeneity within cells but may differ across cells.

2.6 The Long Edge Problem and Path Monotonicity

Real data graphs frequently contain long edges connecting geometrically distant points that happen to be mutual nearest neighbors. These edges create artifacts in gradient flow computation: a trajectory may follow a single long edge to jump between basins, violating the assumption that flow follows the intrinsic geometry of the data manifold.

We address this through path monotonicity validation. For an edge $e = [i, j]$ with $f(i) < f(j)$, we compute the shortest alternative path $P(i, j)$ that avoids e . If f increases strictly along $P(i, j)$, the edge respects the underlying monotonicity and participates in gradient flow. If f oscillates along $P(i, j)$, the edge creates an artificial shortcut and we exclude it from flow computation, requiring trajectories to follow longer but geometrically faithful paths.

Formally, we define the validated edge set

$$E_{\text{val}} = \{[i, j] \in E : f \text{ is monotone along } P(i, j)\} \quad (13)$$

and compute gradient flow using only edges in E_{val} . This removes spurious connections while preserving genuine geometric structure.

The path monotonicity criterion has theoretical justification. If the function f truly varies smoothly along the data manifold, then any edge connecting points with $f(i) < f(j)$ should lie in a region where f increases throughout. The existence of a non-monotone alternative path indicates that the direct edge cuts across level sets rather than following the manifold geometry, suggesting that it represents noise in the k-nearest neighbor construction rather than intrinsic structure.

2.7 Spectral Filtering and Conditional Expectation Estimation

Given observed outcomes y_1, \dots, y_n , we estimate the conditional expectation $E[Y|X]$ through spectral filtering on the graph Laplacian. The empirical vertex function $y = (y_1, \dots, y_n)$ contains both signal (the true conditional expectation) and noise. Spectral methods decompose y into components corresponding to different geometric frequencies on the graph.

We begin with the eigendecomposition $L_{\text{norm}} = V\Lambda V^T$, where Λ is diagonal with eigenvalues $0 = \lambda_1 \leq \lambda_2 \leq \dots \leq \lambda_n \leq 2$ and V contains the corresponding eigenvectors. The eigenvector v_1 associated with $\lambda_1 = 0$ is constant (proportional to $M_0^{1/2}\mathbf{1}$), while eigenvectors associated with small positive eigenvalues vary slowly across edges, and eigenvectors with large eigenvalues oscillate rapidly.

The smoothed estimate takes the form

$$\hat{y} = \sum_{i=1}^n h(\lambda_i) \langle y, v_i \rangle v_i, \quad (14)$$

where $h : [0, 2] \rightarrow [0, 1]$ is a spectral filter that attenuates high-frequency components. We employ the heat kernel filter $h(\lambda) = \exp(-t\lambda)$, which corresponds to solving the heat equation for time t :

$$\hat{y} = \exp(-tL_{\text{norm}})y. \quad (15)$$

The diffusion time t controls smoothness: small t yields estimates close to the empirical values, while large t produces heavily smoothed estimates. We select t through generalized cross-validation or by monitoring convergence of the gradient flow structure: we increase t until the number and prominence of local extrema stabilize.

This spectral approach has several advantages over local smoothing methods. It naturally adapts to the graph geometry, diffusing rapidly within well-connected regions and slowly across sparse connections. It respects the Riemannian structure encoded in M_0 and M_1 , ensuring that smoothing follows the intrinsic manifold rather than the ambient Euclidean space. It enables efficient computation through sparse matrix methods and iterative eigensolvers, scaling to graphs with thousands of vertices.

2.8 Summary of the Geometric Framework

We have constructed a complete framework for representing and analyzing functions on data-derived graphs. The Riemannian structure (M_0, M_1) encodes local density and geometric relationships through vertex and edge masses. The graph Laplacian L_0 governs diffusion and enables spectral filtering for robust estimation. The discrete gradient provides a natural notion of directional derivative, leading to gradient flow trajectories and basin decomposition. Path monotonicity validation removes artifactual long edges, ensuring that gradient flow follows the intrinsic data geometry.

This geometric perspective transforms the statistical inference problem. Rather than estimating $E[Y|X]$ in the ambient Euclidean space \mathbb{R}^d , we estimate a function on the graph $G(X)$ and partition the graph into regions of monotonic behavior through gradient flow

analysis. The partition emerges from the geometry rather than being imposed a priori, and the Riemannian structure ensures that inference respects the intrinsic dimensionality and density variation of the data.

We now proceed to develop the complete inference framework: identification and filtering of spurious extrema, clustering of basins to manage over-segmentation, and introduction of co-monotonicity measures for association analysis within gradient flow cells.

3. The Long Edge Problem and Path Monotonicity Validation

Real data-derived graphs pose a fundamental challenge for discrete gradient flow computation: the k-nearest neighbor construction that makes the graph computationally tractable simultaneously introduces edges that violate the geometric principles underlying gradient trajectories. We confront the question of why naive gradient flow fails on realistic graphs and develop a path-based validation criterion that restores geometric faithfulness without requiring expensive global computations.

3.1 The Challenge of Long Edges

Consider constructing a k-nearest neighbor graph from a sample drawn from a low-dimensional manifold embedded in high-dimensional space. The standard construction connects each point to its k nearest neighbors by Euclidean distance in the ambient space, creating edges that respect local density but potentially violate global geometry. When the manifold curves or has boundaries, points that are close in Euclidean distance may lie far apart along the manifold. A point near the edge of a curved region might have as its k-th nearest neighbor a point on the opposite side of a valley, leading to an edge that shortcuts across the manifold rather than following its intrinsic geometry.

These long edges are necessary for graph connectivity. Without them, the graph fragments into components corresponding to dense regions, preventing paths between different parts of the sample. Yet these same edges create artifacts in gradient flow computation. Consider a vertex v in a descending basin of a local minimum m , where the smoothed function \hat{y} decreases monotonically along all paths through neighboring vertices toward m . If v has a long edge to a vertex u in a different basin where $\hat{y}(u) < \hat{y}(v)$, the naive gradient rule (follow the neighbor with minimal function value) directs the trajectory to jump across basins, violating the fundamental property that gradient flow should follow monotone paths along the underlying geometry.

We illustrate this phenomenon through a concrete example. Let M be a manifold in \mathbb{R}^2 consisting of two crescents separated by a narrow gap, with a function $f : M \rightarrow \mathbb{R}$ having a local minimum in each crescent. Dense sampling near the crescent tips yields k-nearest neighbor graphs with edges connecting the two components. For a vertex v near one crescent tip, its nearest neighbors in the ambient Euclidean metric include points across the gap in the other crescent, despite the manifold distance being substantially larger.

When v lies in the basin of minimum m_1 in the first crescent, but has a neighbor u in the basin of minimum m_2 in the second crescent with $\hat{y}(u) < \hat{y}(v)$, the naive gradient trajectory jumps from basin to basin, producing what we term basin jumping artifacts.

3.2 Inadequacy of Existing Approaches

One might attempt to resolve this issue through the Hodge Laplacian gradient, which incorporates global geometric information through the mass matrices. Recall that the discrete gradient of a function $y : V \rightarrow \mathbb{R}$ can be computed as a 1-chain (function on edges) via

$$(\nabla y)_e = [M_1^{-1} B_1^T M_0 y]_e, \quad (16)$$

where $B_1 : \mathbb{R}^E \rightarrow \mathbb{R}^V$ is the coboundary operator, M_0 is the vertex mass matrix, and M_1 is the edge mass matrix encoding the Riemannian metric. This gradient assigns to each edge a value that reflects not merely the local function difference but the edge's role in the global geometric structure.

The edge mass $M_1[e, e]$ for an edge $e = [i, j]$ quantifies the overlap between the k -neighborhoods of vertices i and j , with larger mass indicating stronger geometric connection. Long edges connecting distant points have small mass (small neighborhood overlap), and the inverse M_1^{-1} amplifies their contribution, potentially destabilizing the gradient computation. While this approach implicitly downweights long edges through their small mass values, it provides only an indirect solution. Computing the Hodge gradient requires solving a linear system involving M_1^{-1} , which can be ill-conditioned when edge masses vary over several orders of magnitude, a common occurrence in real data where sampling density fluctuates. Moreover, the spectral properties of M_1 do not directly enforce the path monotonicity that characterizes true gradient trajectories.

Alternatively, one might restrict gradient flow computation to edges shorter than a quantile threshold τ_q , where τ_q is the q -quantile of the edge length distribution for some $q \in [0.5, 1]$. This heuristic removes the most problematic edges but discards potentially valid geometric information. A long edge might legitimately connect vertices that lie on a genuine gradient trajectory if the underlying function varies smoothly between them. Uniform length thresholding cannot distinguish between geometrically faithful long edges and artifactual ones, leading to unnecessary loss of connectivity and potential fragmentation of basins.

3.3 Path Monotonicity as a Validation Criterion

We return to the defining property of gradient trajectories in smooth Morse theory. Let $f : M \rightarrow \mathbb{R}$ be a smooth function on a Riemannian manifold M , and let $\gamma : [0, 1] \rightarrow M$ be a gradient trajectory with $\gamma(0) = p$ and $\gamma(1) = q$. By definition, $\gamma'(t) = \nabla f(\gamma(t))$ for all t , where ∇f is the Riemannian gradient. This implies that f varies monotonically along γ :

$$\frac{d}{dt} f(\gamma(t)) = \langle \nabla f(\gamma(t)), \gamma'(t) \rangle = \|\nabla f(\gamma(t))\|^2 > 0, \quad (17)$$

assuming γ does not pass through critical points. The function increases strictly along ascending trajectories and decreases strictly along descending trajectories. This monotonicity is not merely a local property at each point but a global constraint on the entire path.

In the discrete setting, we translate this insight into an operational criterion. For an edge $e = [i, j]$ to participate in gradient flow, we require not only that the function increases from i to j (for ascending flow) but that the increase reflects genuine geometric variation rather than artificial jumping across the manifold. We validate this by examining alternative paths: if the function truly varies smoothly in the region containing i and j , then any path connecting them should exhibit consistent monotonic behavior.

Definition 9 (Path Monotonicity). Let $\gamma = (v_0, v_1, \dots, v_k)$ be a path in G with $v_0 = i$ and $v_k = j$. The function \hat{y} is monotone along γ if for all $\ell \in \{0, 1, \dots, k-1\}$ we have $\hat{y}(v_{\ell+1}) > \hat{y}(v_\ell)$ for ascending monotonicity, or $\hat{y}(v_{\ell+1}) < \hat{y}(v_\ell)$ for descending monotonicity. We quantify the degree of monotonicity through the co-monotonicity coefficient along the path:

$$\text{cm}(\hat{y}; \gamma) = \frac{\sum_{\ell=0}^{k-1} w_{v_\ell v_{\ell+1}} \Delta_{v_\ell v_{\ell+1}} \hat{y}}{\sum_{\ell=0}^{k-1} w_{v_\ell v_{\ell+1}} |\Delta_{v_\ell v_{\ell+1}} \hat{y}|}, \quad (18)$$

where $\Delta_{v_\ell v_{\ell+1}} \hat{y} = \hat{y}(v_{\ell+1}) - \hat{y}(v_\ell)$ and $w_{v_\ell v_{\ell+1}}$ are edge weights. For strictly monotone paths, $\text{cm}(\hat{y}; \gamma) = 1$ for ascending paths and $\text{cm}(\hat{y}; \gamma) = -1$ for descending paths.

The path co-monotonicity coefficient aggregates signed differences along the path, normalized by total variation. Perfect monotonicity yields $\text{cm}(\hat{y}; \gamma) = \pm 1$, while oscillating functions produce values closer to zero. We employ this coefficient to define a validation procedure for long edges.

For an edge $e = [i, j]$ with edge length Δ_e exceeding a threshold τ_q (typically the q -quantile of edge lengths for $q \in [0.75, 0.90]$), we compute the shortest alternative path $P(i, j)$ that avoids e . If no such path exists, the edge is essential for connectivity and we accept it by default. If $P(i, j)$ exists, we evaluate $\text{cm}(\hat{y}; P(i, j))$ and compare against a threshold $\theta \in [0.85, 1.0]$. For ascending flow, we require $\text{cm}(\hat{y}; P(i, j)) \geq \theta$; for descending flow, $\text{cm}(\hat{y}; P(i, j)) \leq -\theta$. The edge participates in gradient flow only if this monotonicity condition holds.

Definition 10 (Validated Edge Set). Given a function $\hat{y} : V \rightarrow \mathbb{R}$, a quantile threshold q , and a monotonicity threshold θ , the validated edge set for ascending flow is

$$E_{\text{val}}^\uparrow = \{[i, j] \in E : \Delta_e \leq \tau_q \text{ or } \text{cm}(\hat{y}; P(i, j)) \geq \theta\}, \quad (19)$$

and similarly for descending flow with $\text{cm}(\hat{y}; P(i, j)) \leq -\theta$. We compute gradient trajectories using only edges in E_{val}^\uparrow for ascending basins and $E_{\text{val}}^\downarrow$ for descending basins.

This criterion captures the essential geometric property of gradient trajectories while remaining computationally tractable. Computing the shortest alternative path requires breadth-first search after temporarily removing edge e , an $O(|E|)$ operation for sparse graphs. Evaluating path monotonicity involves a single pass through the path vertices, adding negligible overhead. The total cost of validating all long edges is $O(L \cdot |E|)$ where L is the number of long edges, typically a small fraction of $|E|$ for well-chosen q .

3.4 Theoretical Justification

We provide an informal justification for why path monotonicity validation recovers geometrically faithful gradient flow in the limit of dense sampling. The argument relies on the manifold hypothesis and general position properties of sampled points.

Suppose the data $X_n = \{x_1, \dots, x_n\}$ are sampled from a smooth probability distribution supported on a d -dimensional manifold M embedded in \mathbb{R}^D , and let $f : M \rightarrow \mathbb{R}$ be a smooth function with non-degenerate critical points. For sufficiently large n and appropriate choice of $k = k(n)$ growing with n but satisfying $k/n \rightarrow 0$, the k -nearest neighbor graph G_n approximates the manifold M in the sense that geodesic distances on G_n converge to manifold distances on M .

Consider an edge $e = [i, j]$ in G_n connecting points $x_i, x_j \in M$ with $f(x_i) < f(x_j)$. If this edge lies on a gradient trajectory of f , then the curve segment connecting x_i to x_j follows the gradient direction, implying that f increases monotonically between them. For dense sampling, the shortest path $P(i, j)$ in G_n (excluding edge e) approximates a curve on M close to the direct connection. Since f varies continuously and increases throughout the region, the function values along $P(i, j)$ increase monotonically as well, yielding $\text{cm}(\hat{y}; P(i, j)) \approx 1$.

Conversely, suppose edge e creates a shortcut across a valley in the function landscape. The edge connects x_i and x_j that are close in Euclidean distance but separated by a region where f first decreases then increases. The alternative path $P(i, j)$ must traverse this valley, encountering vertices where \hat{y} first decreases from $\hat{y}(x_i)$ then increases to $\hat{y}(x_j)$. This oscillation yields $\text{cm}(\hat{y}; P(i, j)) < \theta$ for reasonable thresholds θ , causing the validation to reject the edge.

The threshold $\theta < 1$ provides robustness to sampling noise and discretization effects. In practice, $\theta \in [0.85, 0.95]$ accommodates small oscillations due to finite sample size while maintaining the essential monotonicity requirement. The quantile threshold q balances between preserving connectivity and filtering artifacts, with $q \in [0.75, 0.90]$ typically appropriate for k -nearest neighbor graphs where most edges are short and only the tail of the length distribution contains problematic edges.

3.5 Basin Computation with Validated Gradient Flow

We now describe how validated edges integrate into the basin computation algorithm. The construction proceeds through breadth-first exploration from each local extremum, accepting vertices into the basin only when they satisfy the appropriate monotonicity condition along paths from the extremum.

For a local maximum M , we construct the descending basin $D(M)$ through the following procedure. Initialize the basin with $D(M) = \{M\}$ and a queue with M . Maintain a distance map recording the hop distance from M and a predecessor map tracking paths. While the queue is non-empty, dequeue a vertex $u \in D(M)$ and examine each neighbor $v \notin D(M)$. If $\hat{y}(v) < \hat{y}(u)$ (descending condition), check whether the edge $[u, v]$ requires validation (length $\Delta_{uv} > \tau_q$). For short edges, accept v immediately. For long edges,

compute the shortest alternative path $P(u, v) \setminus \{u\}$ from u to v excluding the direct edge, and evaluate $\text{cm}(\hat{y}; P(u, v))$. If $\text{cm}(\hat{y}; P(u, v)) \leq -\theta$, the edge is validated and we accept v into the basin, setting its predecessor to u and adding it to the queue. If validation fails, we reject this edge and continue examining other neighbors of u .

The algorithm ensures that every vertex in $D(M)$ is connected to M through a path where function values decrease monotonically. Vertices reachable only through invalidated long edges remain outside the basin, even if they would be included under naive gradient flow. This prevents basin jumping while maintaining computational tractability through lazy evaluation: we validate edges only when they arise in the breadth-first search, avoiding exhaustive validation of the entire graph.

Algorithm 1 Validated Descending Basin Computation

Input: Graph $G = (V, E)$, function $\hat{y} : V \rightarrow \mathbb{R}$, local maximum M , quantile q , threshold θ

Output: Basin $D(M) \subseteq V$

Compute edge length quantile $\tau_q = \text{quantile}(\{\Delta_e : e \in E\}, q)$

Initialize $D(M) \leftarrow \{M\}$, queue $\leftarrow [M]$, $\text{dist}[M] \leftarrow 0$, $\text{pred}[M] \leftarrow \text{null}$

```

while queue not empty do
   $u \leftarrow \text{dequeue}()$ 
  for each neighbor  $v$  of  $u$  do
    if  $v \notin D(M)$  and  $\hat{y}(v) < \hat{y}(u)$  then
       $e \leftarrow [u, v]$ 
      if  $\Delta_e \leq \tau_q$  then
        valid  $\leftarrow$  true {Short edge, accept}
      else
         $P \leftarrow \text{ShortestPath}(u, v, G \setminus \{e\})$ 
        if  $P = \emptyset$  then
          valid  $\leftarrow$  true {Essential for connectivity}
        else
          valid  $\leftarrow$   $\text{cm}(\hat{y}; P) \leq -\theta$  {Check monotonicity}
        end if
      end if
      if valid then
         $D(M) \leftarrow D(M) \cup \{v\}$ 
         $\text{dist}[v] \leftarrow \text{dist}[u] + 1$ 
         $\text{pred}[v] \leftarrow u$ 
        enqueue( $v$ )
      end if
    end if
  end for
end while
return  $D(M)$ 

```

Ascending basins for local minima follow the same structure with reversed inequality con-

ditions: we accept neighbors v with $\hat{y}(v) > \hat{y}(u)$ and require $\text{cm}(\hat{y}; P(u, v)) \geq \theta$ for long edges. The complete partition of vertices into basins emerges from running this algorithm for all detected local extrema, with ambiguous vertices (reachable from multiple extrema) assigned through tie-breaking rules based on path length and function value differences.

3.6 Computational Complexity and Practical Implementation

The computational cost of validated basin computation scales with the number of long edges requiring validation. Let $n = |V|$ denote the number of vertices, k the neighborhood size in the k -nearest neighbor graph, and L the number of long edges exceeding threshold τ_q . For each long edge, computing the shortest alternative path requires breadth-first search with cost $O(nk)$ in the worst case, though typical paths have length $O(k)$ leading to expected cost $O(k^2)$ per validation. With L long edges, total validation cost is $O(Lk^2)$.

Since L is typically a small fraction of total edges (for $q = 0.75$, we have $L = 0.25 \cdot nk$), and most validations occur during basin construction where we only examine edges incident to basin vertices, the practical cost is substantially lower than the worst-case bound. We implement several optimizations to improve efficiency further.

First, we cache shortest paths between frequently accessed vertex pairs. When multiple extrema have overlapping neighborhoods, the same alternative paths arise repeatedly during basin computation. A least-recently-used cache with capacity $O(n)$ reduces redundant path computations at the cost of $O(n)$ additional memory.

Second, we relax the strict monotonicity requirement through the threshold θ , avoiding validation failure due to minor numerical fluctuations in the smoothed function \hat{y} . Setting $\theta = 0.90$ accommodates up to 10% of the total variation in non-monotonic differences while maintaining robust filtering of artifactual edges.

Third, we defer validation to the breadth-first search phase rather than pre-computing validity for all edges. This lazy evaluation ensures we validate only edges that actually participate in basin computation, reducing unnecessary work for edges far from extrema.

The edge length quantile τ_q provides a tunable parameter balancing computational cost and geometric accuracy. Smaller q validates fewer edges (faster computation, more aggressive filtering), while larger q validates more edges (slower computation, more conservative filtering). Empirically, $q \in [0.75, 0.85]$ provides good performance across diverse datasets, with the optimal value depending on the intrinsic dimensionality of the data manifold and the smoothness of the outcome function.

3.7 Return to the Motivating Example

We return to the two-crescent example to demonstrate how path monotonicity validation resolves basin jumping. Recall that naive gradient flow produces trajectories jumping between crescents due to long edges connecting their tips. Under validated gradient flow, we examine each such long edge $e = [i, j]$ where i belongs to the first crescent and j to the second.

Computing the shortest alternative path $P(i, j)$ yields a route that must travel along one crescent toward the connecting region, cross to the other crescent, then proceed to the target. For a function with separate minima in each crescent, this path necessarily exhibits non-monotonic behavior: the function decreases from i toward the minimum in the first crescent, increases through the connecting region, then decreases again toward j and its local minimum. The path co-monotonicity coefficient $\text{cm}(\hat{y}; P(i, j))$ captures this oscillation, yielding a value near zero rather than the $-\theta$ required for validation.

The validation procedure rejects these artifactual long edges, forcing gradient trajectories to remain within their respective crescents. Each local minimum now correctly captures all vertices in its crescent, and the basin boundaries align with the geometric separation between regions. The resulting Morse-Smale complex accurately reflects the intrinsic structure of the outcome landscape rather than artifacts of the discrete graph construction.

This path-based approach provides direct enforcement of the defining property of gradient trajectories while remaining computationally practical. The validated basins serve as geometric stratification for subsequent inference, enabling regional analysis that respects the manifold structure underlying the data. We proceed to develop co-monotonicity measures that quantify feature associations within these geometrically faithful regions.

4. Co-Monotonicity Coefficients

Having established gradient flow partitions through validated basins, we turn to quantifying associations between functions on graph vertices. The fundamental question driving this development is: how should we measure whether two functions vary together or oppositely along the edges of a graph? Classical correlation coefficients treat all observations as equally related, ignoring the geometric structure encoded by the graph. We seek measures that respect this structure, detecting directional concordance locally while adapting to spatial heterogeneity in association patterns.

4.1 The Inadequacy of Global Association Measures

Consider an outcome function $y : V \rightarrow \mathbb{R}$ and a potential predictor $z : V \rightarrow \mathbb{R}$ defined on the vertices of a graph $G = (V, E)$ derived from high-dimensional data. Standard correlation analysis computes the Pearson coefficient

$$\rho(y, z) = \frac{\text{Cov}(y, z)}{\sigma_y \sigma_z} = \frac{\sum_{v \in V} (y(v) - \bar{y})(z(v) - \bar{z})}{\sqrt{\sum_{v \in V} (y(v) - \bar{y})^2} \sqrt{\sum_{v \in V} (z(v) - \bar{z})^2}}, \quad (20)$$

where \bar{y} and \bar{z} denote sample means. This measure treats all vertex pairs equally, implicitly assuming that observations at vertices v and u are as related as observations at v and w , regardless of whether edges connect these pairs in the graph. When the graph encodes meaningful proximity relationships, as in spatial data or network analysis, this assumption discards valuable structural information.

Moreover, correlation measures linear association in terms of deviations from means, which may not align with the geometric properties of interest. Within a gradient flow cell where

the outcome \hat{y} varies monotonically, we seek features that exhibit monotone co-variation along the same paths, increasing when \hat{y} increases and decreasing when \hat{y} decreases. A feature z that oscillates around a constant mean but always changes in the same direction as \hat{y} across edges would receive zero Pearson correlation despite perfect directional concordance.

Mutual information and related entropy-based measures address nonlinearity but require density estimation in high dimensions, introducing computational expense and methodological complexity. For large graphs with thousands of vertices, estimating joint distributions becomes impractical. We require computationally efficient measures that capture directional relationships while respecting graph geometry.

4.2 Edge-Based Directional Concordance

We begin by formalizing the notion of directional agreement along a single edge. Let $e = [i, j] \in E$ be an edge connecting vertices i and j , and define the edge difference operator acting on a function $f : V \rightarrow \mathbb{R}$ by

$$\Delta_e f = f(j) - f(i). \tag{21}$$

This operator measures the change in f when moving from i to j along edge e . The orientation of edges is arbitrary; what matters is that we consistently use the same orientation for all functions when computing products of differences.

The product $\Delta_e y \cdot \Delta_e z$ captures the directional concordance of y and z along edge e . When both functions increase ($\Delta_e y > 0$ and $\Delta_e z > 0$) or both decrease ($\Delta_e y < 0$ and $\Delta_e z < 0$), the product is positive, indicating co-monotonic behavior. When the functions change in opposite directions, the product is negative, indicating anti-monotonic behavior. When at least one function remains constant across the edge, the product vanishes.

To illustrate these concepts, consider a one-dimensional example where vertices lie on a line and edges connect adjacent points. Let $y(v)$ represent temperature at position v , and $z(v)$ represent humidity. If temperature and humidity both increase as we move along the line (both functions have positive derivatives), then $\Delta_e y \cdot \Delta_e z > 0$ for all edges e , reflecting strong positive co-monotonicity. If temperature increases while humidity decreases, the products are negative, indicating negative co-monotonicity. If temperature increases in some regions and decreases in others, while humidity varies independently, the products will have mixed signs, and we require aggregation over neighborhoods to assess overall association.

4.3 Vertex-Level Co-Monotonicity Coefficients

We aggregate edge-wise directional concordance over neighborhoods to obtain vertex-level measures. At each vertex v , let $N(v)$ denote the set of neighbors (vertices connected to v by edges). We sum the products $\Delta_e y \cdot \Delta_e z$ over all edges incident to v , weighting by edge-specific factors $w_e \geq 0$, and normalize by the total weighted absolute co-variation.

Definition 11 (Vertex-Level Co-Monotonicity Coefficient). Given functions $y, z : V \rightarrow \mathbb{R}$ on a weighted graph $G = (V, E)$ with edge weights $w_e \geq 0$, the co-monotonicity coefficient at vertex v is

$$\text{cm}(y, z; w)(v) = \frac{\sum_{u \in N(v)} w_e \Delta_e y \cdot \Delta_e z}{\sum_{u \in N(v)} w_e |\Delta_e y \cdot \Delta_e z|}, \quad (22)$$

where $e = [v, u]$ is the edge connecting v and u , and $\Delta_e y = y(u) - y(v)$, $\Delta_e z = z(u) - z(v)$. When the denominator vanishes (all products $\Delta_e y \cdot \Delta_e z = 0$), we define $\text{cm}(y, z; w)(v) = 0$.

The normalization ensures that $\text{cm}(y, z; w)(v) \in [-1, 1]$ for all vertices. Perfect positive co-monotonicity (both functions always change in the same direction within the neighborhood) yields $\text{cm}(y, z; w)(v) = 1$. Perfect negative co-monotonicity (functions always change in opposite directions) yields $\text{cm}(y, z; w)(v) = -1$. Values near zero indicate no systematic directional relationship, either because the functions vary independently or because positive and negative concordance balance within the neighborhood.

This vertex-level formulation provides spatially-resolved information about where in the graph the two functions are most strongly associated. Unlike global correlation, which reduces all vertex pairs to a single number, co-monotonicity coefficients reveal regional structure in association patterns. In microbiome applications, this enables identification of samples where particular phylotypes exhibit strong co-variation with outcomes, while other samples show weak or opposite associations.

4.4 Weighting Schemes and Geometric Interpretations

The edge weights w_e control how we aggregate directional concordance over neighborhoods. Three canonical weighting schemes address different geometric and statistical contexts.

The simplest choice assigns uniform weight to all edges: $w_e = 1$ for all $e \in E$. This unit weighting scheme treats edges equally regardless of their length, emphasizing the combinatorial structure of the graph. The coefficient $\text{cm}(y, z; 1)(v)$ counts the proportion of edges where functions agree in direction, providing a robust summary insensitive to the magnitude of changes. Unit weighting is appropriate when edge lengths are roughly comparable, as in regular lattices, or when we wish to count directional agreements without geometric normalization. For graphs constructed from irregular spatial samples where edge lengths vary substantially, unit weighting may overweight long edges that span large distances in the underlying space.

To account for geometric scaling, we introduce derivative weighting. Let Δ_e denote the length (or weight) of edge e in the graph metric. Setting $w_e = 1/\Delta_e^2$ normalizes the coefficient to compare directional derivatives rather than absolute changes:

$$\text{cm}_\partial(y, z)(v) = \frac{\sum_{u \in N(v)} \frac{1}{\Delta_e^2} \Delta_e y \cdot \Delta_e z}{\sum_{u \in N(v)} \frac{1}{\Delta_e^2} |\Delta_e y \cdot \Delta_e z|} = \frac{\sum_{u \in N(v)} \frac{\Delta_e y}{\Delta_e} \cdot \frac{\Delta_e z}{\Delta_e}}{\sum_{u \in N(v)} \left| \frac{\Delta_e y}{\Delta_e} \cdot \frac{\Delta_e z}{\Delta_e} \right|}. \quad (23)$$

The quantities $\Delta_e y / \Delta_e$ and $\Delta_e z / \Delta_e$ approximate directional derivatives along edge e , making $\text{cm}_\partial(y, z)(v)$ analogous to measuring correlation between gradients in the continuous

setting. Derivative weighting naturally mitigates the influence of long edges: a large change $\Delta_e y$ across a long edge Δ_e corresponds to a small derivative $\Delta_e y / \Delta_e$, reducing its contribution to the coefficient. This weighting is appropriate when functions represent continuous quantities sampled at irregular positions, and we wish to assess co-variation in the underlying continuous fields.

For robustness to outliers and heavy-tailed distributions, sign-based weighting uses only the direction of change, discarding magnitude information entirely. We modify the definition slightly, replacing weighted sums with counts:

$$\text{cm}_{\pm}(y, z)(v) = \frac{\sum_{u \in N(v)} \text{sign}(\Delta_e y \cdot \Delta_e z)}{|N(v)|}, \quad (24)$$

where $\text{sign}(x) = 1$ if $x > 0$, $\text{sign}(x) = -1$ if $x < 0$, and $\text{sign}(0) = 0$. This coefficient measures the proportion of edges where functions agree in direction minus the proportion where they disagree. Sign-based weighting is insensitive to the magnitude of function changes, making it robust to outliers or to situations where only ordinal relationships are meaningful. It trades geometric precision for statistical robustness.

4.5 Connection to Angular Correlation of Gradients

We provide an informal argument connecting derivative-weighted co-monotonicity to geometric quantities on smooth manifolds. Suppose data $X = \{x_1, \dots, x_n\}$ are sampled from a smooth Riemannian manifold M , and let $y, z : M \rightarrow \mathbb{R}$ be smooth functions. The k -nearest neighbor graph G_n constructed from X approximates M in the limit of dense sampling with appropriate choice of $k = k(n)$.

For a vertex v corresponding to point $x_v \in M$, the neighborhood $N(v)$ consists of points approximately uniformly distributed in a geodesic ball of radius r_k around x_v , where r_k is the distance to the k -th nearest neighbor. The edge difference $\Delta_e y / \Delta_e$ for an edge $e = [v, u]$ approximates the directional derivative of y in the direction from x_v to x_u :

$$\frac{\Delta_e y}{\Delta_e} \approx \langle \nabla_M y(x_v), \xi_e \rangle, \quad (25)$$

where ξ_e is the unit tangent vector at x_v pointing toward x_u , and $\nabla_M y$ is the Riemannian gradient of y on M . Similarly, $\Delta_e z / \Delta_e \approx \langle \nabla_M z(x_v), \xi_e \rangle$.

The numerator of $\text{cm}_{\partial}(y, z)(v)$ becomes a Riemann sum approximating an integral over directions:

$$\sum_{u \in N(v)} \frac{\Delta_e y}{\Delta_e} \cdot \frac{\Delta_e z}{\Delta_e} \approx \int_{S_{x_v}} \langle \nabla_M y(x_v), \xi \rangle \langle \nabla_M z(x_v), \xi \rangle d\sigma(\xi), \quad (26)$$

where S_{x_v} is the unit sphere in the tangent space $T_{x_v} M$ and $d\sigma$ is the uniform measure. Evaluating this integral yields

$$\int_{S_{x_v}} \langle \nabla_M y(x_v), \xi \rangle \langle \nabla_M z(x_v), \xi \rangle d\sigma(\xi) = C_d \langle \nabla_M y(x_v), \nabla_M z(x_v) \rangle, \quad (27)$$

where $C_d > 0$ is a dimension-dependent constant arising from integrating products of directional projections over the sphere. The denominator undergoes similar approximation, leading to

$$\lim_{n \rightarrow \infty} \text{cm}_\partial(y, z)(v) = \frac{\langle \nabla_M y(x_v), \nabla_M z(x_v) \rangle}{|\nabla_M y(x_v)| \cdot |\nabla_M z(x_v)|}, \quad (28)$$

the cosine of the angle between the gradients of y and z at point x_v .

This limiting interpretation reveals that derivative-weighted co-monotonicity measures the directional alignment of gradients in the underlying continuous geometry. Functions with parallel gradients (angle near zero) have co-monotonicity near +1, functions with anti-parallel gradients (angle near π) have co-monotonicity near -1, and functions with orthogonal gradients (angle near $\pi/2$) have co-monotonicity near zero. This geometric perspective explains why derivative weighting is natural for smooth functions on manifolds: it captures intrinsic geometric association independent of the coordinate system used to represent the data.

4.6 Matrix Extension for Multivariate Analysis

In practice, we rarely analyze a single predictor in isolation. Microbiome studies measure hundreds of bacterial taxa, genomic studies measure thousands of genes, and network data involve numerous node attributes. We require efficient computation of co-monotonicity between an outcome and multiple features, as well as among features themselves.

Let $y : V \rightarrow \mathbb{R}$ be an outcome function and $Z = [z_1, \dots, z_m] : V \rightarrow \mathbb{R}^m$ be a matrix of m feature functions. The co-monotonicity matrix between y and Z is the $n \times m$ matrix

$$\text{CM}(y, Z) = [\text{cm}(y, z_j; w)(v)]_{v \in V, j=1, \dots, m}, \quad (29)$$

where each column j contains the vertex-wise co-monotonicity coefficients between y and feature z_j . This matrix provides association profiles: row v shows how all features associate with the outcome in the neighborhood of vertex v , while column j shows the spatial pattern of association for feature z_j across all vertices.

Computing $\text{CM}(y, Z)$ naively by m independent calls to the pairwise co-monotonicity function would redundantly recompute edge differences $\Delta_e y$ for each feature. We optimize by precomputing these y -dependent quantities once, then reusing them across all features. The algorithm maintains edge weights w_e and differences $\Delta_e y$ in memory, iterates over features z_j , and for each feature computes $\Delta_e z_j$ and accumulates weighted products. This reduces computational cost from $O(m \cdot |E|)$ operations performed independently to $O(|E| + m \cdot |E|)$ with shared overhead, approximately halving the runtime for large m .

For feature-feature associations, we compute the tensor

$$\text{CM}(Z, Z) = [\text{cm}(z_j, z_k; w)(v)]_{v \in V, j, k=1, \dots, m}, \quad (30)$$

which is an $n \times m \times m$ object containing co-monotonicity between all pairs of features at all vertices. The slice $\text{CM}(Z, Z)[v, :, :]$ is an $m \times m$ matrix showing how features co-vary in the neighborhood of vertex v . This captures local correlation structure in the feature space,

revealing whether features cluster into modules that vary coherently or whether feature relationships differ across regions of the graph.

In applications, we often augment $\text{CM}(y, Z)$ with selected columns from $\text{CM}(Z, Z)$ to form an extended association profile. For a vertex v , this profile includes both $\text{cm}(y, z_j)(v)$ for all features j and $\text{cm}(z_j, z_k)(v)$ for pairs (j, k) of interest. These profiles embed vertices into an association space where proximity reflects similarity in how outcome and features relate locally. Vertices with similar profiles form co-monotonicity cells, which we will explore in subsequent sections as a basis for geometric multiple testing and biclustering.

4.7 Computational Considerations and Implementation

The algorithmic complexity of computing co-monotonicity coefficients is linear in the number of edges for sparse graphs. For a single pair of functions y and z on a graph with n vertices and $|E|$ edges, the algorithm iterates over each vertex, examines its incident edges, and accumulates weighted products. With bounded vertex degree (typical for k -nearest neighbor graphs with fixed k), this yields $O(nk) = O(|E|)$ time complexity. For m features in matrix form, optimized computation requires $O(m \cdot |E|)$ time after initial graph preprocessing. Space complexity is $O(n + |E|)$ for storing the graph plus $O(nm)$ for the result matrix, which is optimal since the output has this size.

For large-scale applications with thousands of vertices and hundreds of features, we employ OpenMP parallelization while maintaining CRAN compliance. The matrix computation naturally parallelizes over features: each column of $\text{CM}(y, Z)$ can be computed independently once the y -dependent quantities are precomputed. We distribute columns across threads, with each thread maintaining its own accumulation buffers to avoid race conditions. The Makevars configuration detects OpenMP support at compile time and enables parallelization on systems where it is available, gracefully degrading to serial computation otherwise.

Special numerical considerations arise in edge cases. When the denominator $\sum_{u \in N(v)} w_e |\Delta_e y \cdot \Delta_e z|$ vanishes, all edge differences have opposite-signed products that exactly cancel, or all products are zero. We define the coefficient as zero in this case, reflecting absence of systematic directional relationship. For derivative weighting with $w_e = 1/\Delta_e^2$, we guard against division by zero for edges with negligible length $\Delta_e < 10^{-10}$, setting $w_e = 0$ for such edges to exclude them from the computation. This arises rarely in practice but prevents numerical instability.

4.8 Applications and Interpretation

Co-monotonicity coefficients support diverse analytical tasks in high-dimensional data analysis. We outline several key applications that motivate the subsequent development of inference frameworks.

For model assessment, we compare smoothed conditional expectation estimates \hat{y} from different methods to observed outcomes y through $\text{cm}(y, \hat{y})$. Higher co-monotonicity indicates better directional fit: the model captures not merely the average level of outcomes but their

local trends and gradients. This diagnostic reveals where models succeed or fail spatially, complementing global metrics like mean squared error.

For feature selection in regression or classification problems, we compute $\text{CM}(y, Z)$ to identify features most concordant with outcomes. Unlike Pearson correlation which measures linear association globally, co-monotonicity assesses directional concordance locally while respecting graph geometry. Features with high co-monotonicity in particular regions may warrant investigation even if their global correlation is modest, as they may drive outcomes in specific contexts.

Within gradient flow cells established through validated basin computation, co-monotonicity provides natural association measures. Since the outcome \hat{y} varies monotonically within each cell by construction, features that exhibit monotone co-variation with \hat{y} within the cell are prime candidates for mechanistic relationships. We restrict co-monotonicity computation to edges within a cell, yielding cell-specific association coefficients that respect the partition structure.

For multivariate feature analysis, the tensor $\text{CM}(Z, Z)$ reveals how feature relationships vary spatially. In microbiome studies, bacterial taxa may exhibit synergistic co-occurrence in some samples and competitive exclusion in others. The vertex-wise feature co-monotonicity matrix $\text{CM}(Z, Z)[v, :, :]$ at each vertex v captures this local correlation structure, enabling identification of context-dependent feature modules through clustering or network analysis.

Finally, co-monotonicity matrices provide embeddings for biclustering and geometric multiple testing. By treating rows of $\text{CM}(y, Z)$ or selected components of $\text{CM}(Z, Z)$ as feature vectors, we embed vertices into an association space where distances reflect similarity in how features relate to outcomes. Clustering this embedding induces a partition into co-monotonicity cells, which we develop formally in subsequent sections as an alternative to gradient flow cells for discovering structure.

These applications share a common theme: moving from global, homogeneous association measures to spatially-resolved, geometry-aware coefficients that respect the structure latent in high-dimensional data. The vertex-level formulation enables detection of regional patterns that global methods would average away, while the matrix extensions provide computational efficiency for high-dimensional feature spaces. We now proceed to develop the statistical inference framework necessary to distinguish genuine associations from sampling noise in these geometry-respecting measures.

5. Statistical Inference for Co-Monotonicity

Having developed co-monotonicity coefficients as geometric measures of directional association, we confront the fundamental inferential question: how should we distinguish genuine associations from artifacts of sampling variability? The vertex-wise nature of co-monotonicity coefficients presents both opportunity and challenge. We obtain spatially resolved information revealing where associations are strongest, but this spatial resolution demands vertex-level inference procedures that respect the graph structure while accounting for multiple comparisons. The standard hypothesis testing framework, with its focus on p -values and frequentist error rates, sits uncomfortably with the Bayesian spectral filtering

that produces smoothed function estimates. We require inference procedures that propagate uncertainty from the estimation stage through to association quantification, providing probabilistic statements about effect sizes rather than merely rejecting null hypotheses.

5.1 The Multiple Testing Challenge

Consider the typical scenario in microbiome-outcome association studies. We have n samples (vertices in the graph G), an outcome $y : V \rightarrow \mathbb{R}$, and m bacterial taxa (features) $Z = [z_1, \dots, z_m] : V \rightarrow \mathbb{R}^m$. After smoothing to obtain \hat{y} and \hat{Z} through spectral filtering, we compute the co-monotonicity matrix $\text{CM}(\hat{y}, \hat{Z}) \in \mathbb{R}^{n \times m}$ with $n \times m$ coefficients. A naive testing procedure would assess each coefficient independently: for each vertex-feature pair (v, j) , test whether $\text{cm}(\hat{y}, z_j)(v)$ differs significantly from zero. This generates nm hypothesis tests, and with typical values $n = 200$ samples and $m = 100$ features, we face 20,000 simultaneous tests.

The multiple testing burden is severe. Even with independent tests, controlling the family-wise error rate at level $\alpha = 0.05$ through Bonferroni correction requires declaring significance only when $p < 0.05/20000 = 2.5 \times 10^{-6}$, a threshold so stringent that only the most extreme associations would be detected. False discovery rate control offers less conservative correction but still penalizes for the sheer number of tests. Moreover, the independence assumption underlying standard FDR procedures fails dramatically in our setting: co-monotonicity coefficients at adjacent vertices are inherently correlated because they aggregate over overlapping neighborhoods. The graph structure induces spatial dependence that standard multiple testing corrections ignore.

Beyond the computational burden of multiple testing, there is a conceptual issue. The classical hypothesis testing framework asks whether we can reject the null hypothesis of no association, yielding binary decisions (reject or fail to reject) with probabilistic error control. Yet in exploratory high-dimensional data analysis, we rarely seek such binary classifications. We wish to identify regions where associations are strongest, quantify the magnitude of these associations with uncertainty bounds, and compare the strength of different feature-outcome relationships. The hypothesis testing paradigm, with its focus on p -values that measure tail probabilities under null distributions, provides limited information for these goals. We require inference methods that directly address probabilistic questions about effect sizes: what is $P(|\text{cm}(\hat{y}, z_j)(v)| > \delta \mid \text{data})$ for scientifically meaningful thresholds δ , rather than merely $P(\text{data} \mid \text{cm} = 0)$?

5.2 Vertex-Wise Permutation Testing

We begin with the classical nonparametric approach to association testing. Permutation tests provide exact finite-sample inference without distributional assumptions, making them particularly appealing for complex data structures. The key insight is that under the null hypothesis of no association between feature z and outcome y , permuting the feature values across vertices should preserve all aspects of the data generation process except the association of interest.

At each vertex v , we test the null hypothesis $H_0^v : \text{cm}(y, z)(v) = 0$, which corresponds to asserting that y and z have no directional relationship in the neighborhood of v . We compute the observed coefficient $c_{\text{obs}}(v) = \text{cm}(\hat{y}, \hat{z})(v)$ using the smoothed estimates. To generate the null distribution, we permute the feature values: let π be a random permutation of $\{1, \dots, n\}$, and define the permuted feature $z^\pi(v_i) = z(v_{\pi(i)})$ for $i = 1, \dots, n$. This permutation breaks any association between z and y while preserving the marginal distribution of z and the graph structure G .

For each permutation π_b with $b = 1, \dots, B$, we smooth the permuted feature to obtain $\hat{z}^{(\pi_b)}$ and compute $c_b(v) = \text{cm}(\hat{y}, \hat{z}^{(\pi_b)})(v)$. The collection $\{c_1(v), \dots, c_B(v)\}$ forms an empirical null distribution for the co-monotonicity coefficient at vertex v under the hypothesis of no association. We compute the two-sided p -value as

$$p(v) = \frac{1 + \#\{b : |c_b(v)| \geq |c_{\text{obs}}(v)|\}}{B + 1}, \quad (31)$$

where the numerator counts permutations yielding coefficients at least as extreme as the observed value, and the denominator includes the observed data itself as one possible permutation.

This vertex-wise permutation procedure respects the graph structure: the permuted features are smoothed using the same spectral filtering as the original data, ensuring that the null distribution reflects the spatial autocorrelation induced by the Laplacian. However, the procedure treats the smoothed outcome \hat{y} as fixed, ignoring the uncertainty in its estimation. When y itself is estimated through spectral filtering of noisy observations, this omission can lead to underestimation of uncertainty and inflated false positive rates.

For multiple testing correction across the n vertices, we employ the Benjamini-Hochberg procedure to control the false discovery rate. Order the p -values as $p_{(1)} \leq p_{(2)} \leq \dots \leq p_{(n)}$, and let k^* be the largest k such that $p_{(k)} \leq (k/n)\alpha$ for target FDR level α . We declare vertices v with $p(v) \leq p_{(k^*)}$ as significant. This procedure controls the expected proportion of false discoveries among the rejected hypotheses, providing a less conservative alternative to family-wise error rate control.

The spatial structure of significant vertices provides additional information. Rather than treating each vertex independently, we identify connected components in the subgraph induced by significant vertices. Isolated significant vertices likely represent false positives that happened to achieve small p -values by chance, while spatially coherent clusters of significant vertices suggest genuine regional associations. We can impose a minimum cluster size threshold, declaring only those significant vertices belonging to clusters of at least k_{\min} vertices as discoveries. This spatial thresholding provides robustness against false positives arising from the multiple testing burden.

5.3 Bayesian Inference via Posterior Sampling

The permutation testing framework, despite its nonparametric appeal, inherits the limitations of the classical hypothesis testing paradigm. We now develop an alternative Bayesian approach that addresses these limitations by treating uncertainty in the smoothed estimates as the primary source of inferential variability.

The spectral filtering procedure that produces smoothed estimates \hat{y} and \hat{Z} from observed data y and Z admits natural Bayesian interpretation. Recall that the filtered estimate takes the form $\hat{y} = VF_\eta(\Lambda)V^T y$, where V contains eigenvectors of the normalized Laplacian, Λ is the diagonal matrix of eigenvalues, and F_η is a spectral filter (such as the heat kernel $F_\eta(\lambda) = \exp(-\eta\lambda)$ or Tikhonov filter $F_\eta(\lambda) = 1/(1 + \eta\lambda)$). This operation corresponds to the posterior mean under a Gaussian prior on spectral coefficients with precision proportional to eigenvalues.

We elaborate this Bayesian perspective through a generative model for the observed data. Suppose the true outcome function $f : V \rightarrow \mathbb{R}$ has spectral representation $f = V\alpha$ for coefficients $\alpha \in \mathbb{R}^m$, where m is the number of eigenvectors retained. The smoothness prior on spectral coefficients is

$$p(\alpha \mid \eta) \propto \exp\left(-\frac{\eta}{2} \sum_{j=1}^m \lambda_j \alpha_j^2\right), \quad (32)$$

which penalizes high-frequency modes (large λ_j) more severely. Given noisy observations $y_v = f(v) + \epsilon_v$ with $\epsilon_v \sim N(0, \sigma^2)$, the posterior distribution over spectral coefficients is Gaussian:

$$\alpha \mid y, \eta \sim N\left((I + \eta\Lambda)^{-1}V^T y, \sigma^2(I + \eta\Lambda)^{-1}\right). \quad (33)$$

The filtered estimate $\hat{y} = VF_\eta(\Lambda)V^T y$ computes the posterior mean when $F_\eta(\lambda) = 1/(1 + \eta\lambda)$. For other filter types, the filtered estimate approximates the posterior mode or mean under related priors. This connection suggests a natural approach to uncertainty quantification: sample from the posterior distribution over spectral coefficients, transform to vertex space, and propagate this uncertainty through the co-monotonicity computation.

However, directly sampling from the spectral coefficient posterior requires estimating the residual variance σ^2 and assumes Gaussian noise, which may not hold for discrete or bounded outcomes. We employ an alternative resampling strategy that induces posterior-like variability without requiring parametric assumptions. The key idea is to perturb the vertex masses in the Riemannian structure through Dirichlet resampling, generating multiple weighted Laplacians that yield different smoothed estimates.

Definition 12 (Dirichlet Resampling for Posterior Uncertainty). Let M_0 be the vertex mass matrix with diagonal entries $M_0[v, v] = \rho_0(v)$. Denote $w = (\rho_0(1)/n, \dots, \rho_0(n)/n)$ as the normalized vertex weights summing to unity. For concentration parameter $\alpha > 0$, we sample

$$w^* \sim \text{Dirichlet}(\alpha w_1, \dots, \alpha w_n), \quad (34)$$

where larger α concentrates the resampled weights near the original weights w , and smaller α allows greater variability. We construct a perturbed mass matrix M_0^* with diagonal entries $M_0^*[v, v] = nw_v^*$, build the corresponding weighted Laplacian L^* , and compute filtered estimates $\hat{y}^* = V^*F_\eta(\Lambda^*)(V^*)^T y$ and $\hat{z}_j^* = V^*F_\eta(\Lambda^*)(V^*)^T z_j$, where V^* and Λ^* come from the eigendecomposition of L^* .

This Dirichlet resampling procedure induces variability in the smoothed estimates through perturbation of the geometric structure itself. Vertices with large mass $\rho_0(v)$ tend to receive

large perturbed mass $M_0^*[v, v]$, but stochastic variation allows for reordering of vertex importance across samples. The resulting ensemble $\{(\hat{y}^{(b)}, \hat{z}^{(b)})\}_{b=1}^B$ for B independent Dirichlet samples approximates a posterior distribution over smoothed functions.

For each posterior sample b , we compute co-monotonicity coefficients $c^{(b)}(v) = \text{cm}(\hat{y}^{(b)}, \hat{z}_j^{(b)})(v)$ at each vertex v and for each feature j . The empirical distribution of $\{c^{(1)}(v), \dots, c^{(B)}(v)\}$ represents the posterior distribution of the co-monotonicity coefficient at vertex v . We construct credible intervals by computing empirical quantiles: the $(1 - \alpha) \times 100\%$ credible interval for $\text{cm}(\hat{y}, z_j)(v)$ is

$$\text{CI}_{1-\alpha}(v) = [q_{\alpha/2}(\{c^{(b)}(v)\}), q_{1-\alpha/2}(\{c^{(b)}(v)\})], \quad (35)$$

where q_p denotes the p -quantile of the empirical distribution.

These Bayesian credible intervals admit direct probability interpretation: given the observed data and the smoothness prior implicit in spectral filtering, there is $(1 - \alpha) \times 100\%$ posterior probability that the true co-monotonicity lies within the interval. This contrasts with frequentist confidence intervals, which make statements about long-run coverage under repeated sampling. For a vertex v where the credible interval excludes zero (say, $\text{CI}_{0.95}(v) = [0.42, 0.71]$), we conclude with high posterior probability that a genuine directional association exists in the neighborhood of v , and the interval quantifies the magnitude of this association.

5.4 Posterior Probabilities for Effect Size Thresholds

Beyond credible intervals, the Bayesian framework enables computation of posterior probabilities for scientifically meaningful thresholds. Rather than testing whether $\text{cm}(\hat{y}, z)(v) = 0$, we ask whether the co-monotonicity exceeds a threshold $\delta > 0$ representing meaningful association strength. For example, in microbiome studies, we might consider $|\text{cm}| > 0.3$ as indicating moderate directional concordance, and $|\text{cm}| > 0.6$ as strong concordance.

The posterior probability that the co-monotonicity at vertex v exceeds threshold δ is estimated from the empirical distribution of posterior samples:

$$P(|\text{cm}(\hat{y}, z)(v)| > \delta \mid \text{data}) \approx \frac{1}{B} \#\{b : |c^{(b)}(v)| > \delta\}. \quad (36)$$

This probability directly quantifies our belief that the association is meaningful, given the data and prior assumptions. A vertex with $P(|\text{cm}| > 0.3 \mid \text{data}) = 0.95$ has high posterior support for at least moderate association, while $P(|\text{cm}| > 0.6 \mid \text{data}) = 0.45$ indicates uncertain evidence for strong association.

This formulation avoids the binary decision problem inherent in hypothesis testing. We need not declare associations as significant or non-significant based on arbitrary α levels; instead, we report posterior probabilities and credible intervals, allowing domain experts to interpret the strength of evidence in context. Moreover, the Bayesian framework naturally handles multiple comparisons without explicit correction procedures. The posterior distribution already accounts for all sources of uncertainty, including estimation variability and the fact that we are simultaneously assessing many vertex-feature pairs. There is no multiplicity penalty in the Bayesian paradigm because we report probabilistic statements about effect sizes rather than making decisions about null hypotheses.

5.5 Comparison of Inference Approaches

The permutation testing and Bayesian posterior sampling approaches address the inferential challenge from fundamentally different perspectives. We summarize their complementary strengths and limitations.

Permutation testing provides distribution-free inference with exact finite-sample control of type I error rates. Under the null hypothesis of no association, the permutation distribution correctly represents the sampling variability of the test statistic, regardless of the underlying data distribution. This makes permutation tests particularly robust in settings where parametric assumptions are dubious. The vertex-wise procedure respects the graph structure by applying the same spectral filtering to permuted features as to the original data. For confirmatory hypothesis testing where strict control of false positive rates is paramount, permutation tests offer theoretical guarantees that Bayesian methods cannot match.

However, permutation testing treats the smoothed outcome \hat{y} as fixed, ignoring uncertainty in its estimation. When y itself arises from noisy observations and requires smoothing, this omission understates the true uncertainty. The resulting p -values may be anticonservative (too small), inflating false positive rates beyond the nominal level. Moreover, permutation testing yields p -values rather than effect size estimates, requiring separate procedures for quantifying association strength with confidence intervals. The multiple testing correction necessary for controlling FDR or FWER across vertices introduces additional complexity and reduces power, particularly when spatial dependence invalidates independence assumptions underlying standard corrections.

Bayesian posterior sampling addresses these limitations by treating estimation uncertainty as the primary source of inferential variability. The Dirichlet resampling procedure perturbs the geometric structure itself, inducing correlated variability across all smoothed functions. This naturally propagates uncertainty from the estimation stage to the association quantification stage, providing credible intervals that reflect both sampling variability and smoothing uncertainty. The resulting inference is more conservative (wider intervals) but also more honest about what the data truly support. The Bayesian framework yields direct probabilistic statements about effect sizes, such as $P(|\text{cm}| > 0.3 \mid \text{data})$, which answer the scientific questions investigators actually care about.

The disadvantage of Bayesian inference is the need to specify the resampling mechanism (the concentration parameter α in Dirichlet sampling) and the interpretation depends on accepting the implicit prior structure. While the Bayesian credible intervals have asymptotically correct frequentist coverage under regularity conditions (the intervals do contain the true parameter with the stated frequency in repeated sampling), this property requires assumptions about the smoothing operator and the data-generating process. For small samples or when these assumptions fail, Bayesian intervals may not achieve nominal coverage.

We recommend a pragmatic approach that leverages both methods. For exploratory analysis and effect size estimation, employ Bayesian posterior sampling to obtain credible intervals and posterior probabilities. The resulting summaries provide rich information about association patterns, enabling investigators to identify regions of strong association, quan-

tify uncertainty, and compare effects across features. For confirmatory testing where false positive control is critical, supplement the Bayesian analysis with permutation tests, applying FDR correction and spatial thresholding to protect against spurious discoveries. The convergence of evidence from both frameworks strengthens confidence in reported associations.

5.6 Handling Spatial Dependence

Both inference approaches must confront the spatial dependence inherent in co-monotonicity coefficients on graphs. Adjacent vertices typically have similar coefficient values because their neighborhoods overlap, creating positive correlation that standard multiple testing procedures ignore. This spatial autocorrelation inflates the effective number of independent tests, making nominal FDR control procedures liberal (actual FDR exceeds target level).

For permutation testing, we can adapt spatial FDR methods developed for neuroimaging and spatial statistics. One approach treats the significant vertices as a spatial point process and controls the false discovery rate accounting for spatial clustering. We compute the expected number of false positive clusters under the null distribution by examining the spatial distribution of significant vertices in permuted data, then calibrate the rejection threshold to achieve the desired spatial FDR. Alternatively, we can employ random field theory, modeling the co-monotonicity surface as a Gaussian random field and deriving familywise error rates for the maximum statistic over connected regions. These methods require assumptions about the spatial correlation structure but provide more powerful inference than Bonferroni correction when correctly specified.

For Bayesian inference, spatial dependence manifests in the posterior distribution of co-monotonicity vectors across vertices. We can examine the posterior covariance between coefficients at different vertices, identifying regions where association patterns are consistently similar across posterior samples. High posterior correlation between nearby vertices supports the interpretation that they belong to a coherent association region rather than representing independent local effects. This spatial coherence can inform downstream analyses such as biclustering, where we seek to partition vertices into regions based on their association profiles.

A pragmatic approach to spatial dependence is cluster-based inference: rather than testing individual vertices, we test connected components of vertices with large coefficients. The null hypothesis becomes "no cluster of associated vertices exists" rather than "no individual vertex is associated." We compute a cluster-level test statistic (such as the sum of co-monotonicity coefficients within the cluster) and generate its null distribution through permutation. This reduces the multiple testing burden from n vertex-level tests to k cluster-level tests where $k \ll n$, and the spatial thresholding inherent in cluster definition provides robustness against isolated false positives.

5.7 Return to the Motivating Challenge

We return to the multiple testing scenario described in the opening: $n = 200$ samples, $m = 100$ features, yielding 20,000 vertex-feature pairs to assess. Under the permutation testing framework with Benjamini-Hochberg FDR control at level $\alpha = 0.05$, we might identify 500 significant pairs, corresponding to roughly 2.5% of the total. These discoveries typically cluster spatially, with certain vertices showing strong association with multiple features and certain features showing strong association across multiple vertices. The spatial thresholding ensures that we report coherent regions rather than scattered individual vertices.

Under the Bayesian framework, we report the full posterior distribution of co-monotonicity coefficients, providing credible intervals for all 20,000 pairs. For a scientist examining feature j , we can visualize the posterior mean $\text{cm}(\hat{y}, z_j)(v)$ across vertices v , shading regions where the 95% credible interval excludes zero. The width of intervals reveals uncertainty: narrow intervals in densely sampled regions with consistent associations, wide intervals in sparse or heterogeneous regions. Rather than a binary classification of significant versus non-significant, we obtain a graduated assessment of association strength and certainty across the entire sample space.

The two approaches yield complementary information. Permutation testing with FDR control provides a specific set of discoveries with guaranteed error rate properties, suitable for reporting in publications and for guiding follow-up experiments where false positive costs are high. Bayesian credible intervals provide nuanced effect size estimates with uncertainty quantification, enabling investigators to prioritize regions for mechanistic investigation based on both the strength of association and the confidence in that strength. Together, these tools enable rigorous yet flexible inference that respects the geometric structure of the data while controlling error rates and propagating uncertainty.

6. Geometric Multiple Testing via Co-Monotonicity Cells

The vertex-wise inference procedures developed in the previous section enable assessment of individual vertex-feature associations, but they address only part of the inferential challenge. When examining co-monotonicity heatmaps from real applications, a striking pattern emerges: coefficients organize into coherent blocks where groups of vertices exhibit similar association patterns with groups of features. This block structure suggests that regional associations operate not through individual vertex-feature pairs but through collective relationships between sample regions and feature modules. We require a framework that discovers this geometric structure directly, partitioning both the sample space and feature space simultaneously to identify co-monotonicity cells where multivariate associations are coherent.

6.1 The Context-Dependent Association Problem

Consider a microbiome study investigating associations between bacterial taxa and spontaneous preterm birth outcomes. We compute the co-monotonicity matrix $\text{CM}(\hat{y}, \hat{Z}) \in \mathbb{R}^{n \times m}$ where rows correspond to samples (vertices in the graph G constructed from high-dimensional feature profiles) and columns correspond to bacterial phylotypes. Figure 3 displays such a matrix from a study of vaginal microbiome composition in pregnant women, with hierarchical clustering applied to both rows and columns to reveal structure.

The heatmap reveals a block pattern that standard vertex-wise testing cannot capture. One block of samples (upper portion) exhibits strong positive co-monotonicity (red) between outcome and certain phylotypes, indicating these bacteria increase when preterm birth risk increases. A different block of samples (middle portion) shows weak or negative association (blue/yellow) between outcome and the same phylotypes. A third block shows intermediate patterns. Similarly, phylotypes organize into modules: certain taxa co-vary strongly with the outcome across specific sample regions but not others, while different taxa exhibit complementary patterns.

This structure poses fundamental challenges for conventional inference approaches. Testing each phylotype separately across all samples conflates the regional signals, potentially concluding that a phylotype shows no global association when in fact it exhibits strong positive association in one region and strong negative association in another. The signals cancel in global analysis, yielding small test statistics and large p -values despite genuine context-dependent effects. Stratifying by known covariates (such as community state type in microbiome studies) helps but requires investigators to specify strata a priori, and may miss finer-scale heterogeneity within nominal strata.

Moreover, examining individual phylotypes ignores valuable information about their collective behavior. If ten phylotypes all show moderate positive co-monotonicity ($\text{cm}(\hat{y}, z_i)(v) \approx 0.5$) in the same sample region, the coherence across multiple features provides stronger evidence for genuine association than any single phylotype achieves alone. The features form a functional module that operates together, and inference should leverage this coordinated behavior. Traditional multiple testing corrections treat each feature independently, applying penalties that ignore the reduced effective number of independent tests when features cluster into modules.

We seek a framework that addresses both challenges simultaneously: discovering regions where associations differ while identifying feature modules that exhibit coordinated relationships with outcomes within those regions. This leads naturally to biclustering, which partitions rows (samples) and columns (features) simultaneously to maximize within-block homogeneity and between-block heterogeneity.

6.2 Co-Monotonicity Embeddings into Association Space

The co-monotonicity matrix $\text{CM}(\hat{y}, \hat{Z})$ provides association information for each vertex-feature pair, but to discover regional structure, we require a representation that captures the complete association profile at each vertex. We construct embeddings that transform

vertices into points in an association space where geometric proximity reflects similarity in how features relate to outcomes.

The simplest embedding uses outcome-feature associations directly. For each vertex v , we form the association profile vector

$$\text{cm}(\hat{y}, \hat{Z})(v) = [\text{cm}(\hat{y}, z_1)(v), \dots, \text{cm}(\hat{y}, z_m)(v)]^T \in \mathbb{R}^m, \quad (37)$$

which concatenates the co-monotonicity coefficients between outcome and all features at vertex v . This m -dimensional vector summarizes how the outcome associates with each feature in the neighborhood of v . Vertices with similar profiles have similar association patterns, while vertices with dissimilar profiles exhibit different feature-outcome relationships.

This outcome-centric embedding captures one aspect of association structure, but it omits information about how features relate to each other. Two vertices might have similar outcome-feature profiles (similar co-monotonicity with \hat{y} for each feature) yet exhibit different inter-feature correlation patterns. In one region, features z_i and z_j might co-vary positively (both increase together), while in another region they vary independently or negatively. These inter-feature relationships reveal mechanistic structure: positively co-monotonic feature pairs may participate in the same biological pathway or competitive network, and regional differences in inter-feature associations indicate distinct underlying processes.

We therefore construct an augmented embedding that incorporates inter-feature associations. For each vertex v , compute the pairwise co-monotonicity $\text{cm}(z_i, z_j)(v)$ for all feature pairs $i < j$, yielding $\binom{m}{2} = m(m-1)/2$ coefficients. Concatenate these with the outcome-feature associations to form the augmented profile

$$\widetilde{\text{cm}}(\hat{y}, \hat{Z})(v) = \begin{bmatrix} \text{cm}(\hat{y}, z_1)(v) \\ \vdots \\ \text{cm}(\hat{y}, z_m)(v) \\ \text{cm}(z_1, z_2)(v) \\ \vdots \\ \text{cm}(z_{m-1}, z_m)(v) \end{bmatrix} \in \mathbb{R}^{m+m(m-1)/2}. \quad (38)$$

This augmented representation has dimension $m + \binom{m}{2} = m(m+1)/2$, which grows quadratically in the number of features. For $m = 100$ features, the augmented embedding has dimension 5,050. While high-dimensional, this representation preserves complete pairwise association structure, enabling discovery of regions where both outcome associations and feature co-variation patterns differ.

The augmented embedding offers several advantages over the outcome-only version. It captures mechanistic information: vertices clustered together in the augmented space share not only similar outcome associations but also similar inter-feature dependencies, suggesting common underlying processes. It enables multi-modal integration: when analyzing multiple feature sets (genomic, proteomic, metabolomic), we can augment the embedding with cross-modal associations, identifying regions where different data types exhibit coordinated relationships. It provides robustness: even when outcome-feature associations are

weak, strong inter-feature structure can drive clustering, revealing latent organization that outcome-only embeddings would miss.

6.3 Graph Construction in Association Space

Given the co-monotonicity embedding $\widetilde{\text{cm}}(\hat{y}, \hat{Z}) : V \rightarrow \mathbb{R}^d$ where $d = m(m + 1)/2$, we construct a new graph $G_k(\text{cm})$ in the association space. For each vertex $v \in V$, we identify its k nearest neighbors in \mathbb{R}^d using Euclidean distance on the embedded coordinates. This yields a graph where edge $[u, v] \in E(G_k(\text{cm}))$ indicates that vertices u and v have similar association profiles, with proximity measured directly in terms of co-monotonicity coefficients rather than in the original high-dimensional feature space.

The choice of k controls the granularity of the induced structure. Small k produces a sparse graph capturing only the most similar association profiles, potentially fragmenting the vertex set into many disconnected components. Large k creates a dense graph where even moderately dissimilar profiles connect, potentially obscuring meaningful distinctions between regions. We employ the same principles developed for the original data graph construction: select k to ensure connectivity while maintaining local geometric fidelity, typically using k proportional to $\log n$ for n vertices.

The graph $G_k(\text{cm})$ provides a geometric representation of association structure. Communities in this graph (densely connected subgraphs with sparse connections between communities) correspond to co-monotonicity cells: regions where vertices exhibit similar association patterns. Unlike the original data graph G , which captures proximity in feature space (microbiome composition, gene expression, etc.), the association graph $G_k(\text{cm})$ captures proximity in association space. Two samples far apart in microbiome composition might be close in association space if bacteria relate to outcomes similarly in both samples, revealing that similar mechanisms operate despite different baseline compositions.

6.4 Community Detection and Biclustering

We apply community detection algorithms to $G_k(\text{cm})$ to partition vertices into regions. The Louvain method provides an efficient modularity-based approach that scales to large graphs and naturally handles hierarchical structure through multi-resolution optimization. Given the graph $G_k(\text{cm})$ with edge weights derived from association profile similarities, the Louvain algorithm iteratively groups vertices to maximize the modularity function

$$Q = \frac{1}{2|E|} \sum_{[u,v] \in E} \left(A_{uv} - \frac{k_u k_v}{2|E|} \right) \delta(c_u, c_v), \quad (39)$$

where A_{uv} is the adjacency matrix, k_u is the degree of vertex u , c_u is the community assignment of u , and δ is the Kronecker delta. This optimization balances within-community edge density against the expected density under a null model, identifying communities more densely connected internally than would occur by chance.

The resulting partition $\{R_1, \dots, R_K\}$ divides vertices into K regions where association profiles are similar within regions and dissimilar between regions. The number of regions

K emerges from the optimization rather than being specified a priori, and the hierarchical nature of Louvain clustering enables exploration of structure at multiple scales by varying the resolution parameter.

To identify feature modules, we transpose the analysis. Compute the similarity between feature columns in $\text{CM}(\hat{y}, \hat{Z})$: features z_i and z_j are similar if their co-monotonicity profiles across vertices $\text{cm}(\hat{y}, z_i)$ and $\text{cm}(\hat{y}, z_j)$ are correlated. This yields a feature similarity matrix that we cluster using hierarchical agglomerative clustering or network community detection. The resulting modules $\{S_1, \dots, S_M\}$ group features that exhibit similar spatial patterns of association with the outcome.

The combination of vertex regions and feature modules defines a bicluster structure $\{(R_j, S_k)\}_{j=1, \dots, K; k=1, \dots, M}$ partitioning the co-monotonicity matrix into $K \times M$ blocks. Each block (R_j, S_k) represents a co-monotonicity cell where vertices in region R_j exhibit coherent associations with features in module S_k . This structure reveals the regional organization of multivariate associations, showing which feature combinations drive outcomes in which sample contexts.

6.5 Bayesian Uncertainty Quantification for Biclusters

The biclustering procedure applied to a single estimate $\text{CM}(\hat{y}, \hat{Z})$ yields a point estimate of the partition structure, but this estimate is uncertain. Different choices of smoothing parameter, different posterior samples from the Bayesian inference framework, or different noise realizations would produce different clusterings. We require uncertainty quantification for the discovered structure itself, characterizing our confidence in the identified regions and modules.

The posterior sampling framework developed in Section 5 provides a natural approach. For each Dirichlet-resampled weight vector $w^{(b)}$ with $b = 1, \dots, B$, we obtain smoothed estimates $\hat{y}^{(b)}$ and $\hat{Z}^{(b)}$, compute the corresponding co-monotonicity matrix $\text{CM}^{(b)}(\hat{y}, \hat{Z})$, and apply the biclustering procedure to obtain partition $\mathcal{P}^{(b)} = \{R_1^{(b)}, \dots, R_{K_b}^{(b)}\}$ of vertices and $\mathcal{S}^{(b)} = \{S_1^{(b)}, \dots, S_{M_b}^{(b)}\}$ of features. The ensemble $\{\mathcal{P}^{(1)}, \dots, \mathcal{P}^{(B)}\}$ represents the posterior distribution over vertex partition structures, and similarly for feature modules.

To summarize this distribution, we compute co-clustering probabilities. For each pair of vertices (u, v) , the posterior probability that they belong to the same region is

$$\pi_v(u, v) = P(u \text{ and } v \text{ in same region} \mid \text{data}) \approx \frac{1}{B} \sum_{b=1}^B \mathbb{I}\{u, v \in R_j^{(b)} \text{ for some } j\}, \quad (40)$$

where $\mathbb{I}\{\cdot\}$ is the indicator function. This probability quantifies our confidence that vertices u and v truly belong together based on their association profiles, accounting for all sources of uncertainty. High co-clustering probability ($\pi_v(u, v) > 0.95$) indicates strong evidence for grouping, while low probability ($\pi_v(u, v) < 0.20$) suggests the vertices belong to different regions.

Similarly, for each pair of features (z_i, z_j) , we compute

$$\pi_f(z_i, z_j) = P(z_i \text{ and } z_j \text{ in same module} \mid \text{data}) \approx \frac{1}{B} \sum_{b=1}^B \mathbb{I}\{z_i, z_j \in S_k^{(b)} \text{ for some } k\}. \quad (41)$$

These co-clustering probabilities enable construction of credible regions and modules. A credible region R at level $1 - \alpha$ satisfies $\pi_v(u, v) \geq 1 - \alpha$ for all pairs $u, v \in R$, meaning we have at least $(1 - \alpha) \times 100\%$ posterior probability that every pair in the region genuinely belongs together. Maximal credible regions (those not properly contained in any larger credible region) provide conservative summaries of the partition structure, reporting only clusters with high posterior support.

We can also examine the posterior distribution over the number of regions and modules. Let $K^{(b)}$ denote the number of regions in posterior sample b . The empirical distribution of $\{K^{(1)}, \dots, K^{(B)}\}$ quantifies uncertainty about the appropriate granularity of the partition. If this distribution concentrates sharply around a single value (say, $K = 5$ with probability 0.90), we have strong evidence for that many regions. If the distribution is diffuse (ranging from $K = 3$ to $K = 10$ with no dominant mode), the data do not provide clear guidance about the resolution, and we should report results at multiple scales.

6.6 Statistical Inference within Co-Monotonicity Cells

Having identified regions $\{R_1, \dots, R_K\}$ and modules $\{S_1, \dots, S_M\}$, we perform statistical inference on the region-module pairs (R_j, S_k) to assess the strength and uncertainty of associations within each cell. The fundamental question is whether features in module S_k exhibit coherent association with the outcome among vertices in region R_j , and if so, how strong is this association.

We define the region-module coherence as the average absolute co-monotonicity within the cell:

$$\tau(R_j, S_k) = \frac{1}{|R_j| \cdot |S_k|} \sum_{v \in R_j} \sum_{i \in S_k} |\text{cm}(\hat{y}, z_i)(v)|. \quad (42)$$

This quantity measures the typical magnitude of association between outcome and features in the module, averaged over vertices in the region. Large $\tau(R_j, S_k)$ indicates strong coherent association, while small $\tau(R_j, S_k)$ suggests weak or inconsistent associations.

For each posterior sample b , we compute $\tau^{(b)}(R_j, S_k)$ using the posterior estimates $\hat{y}^{(b)}$ and $\hat{Z}^{(b)}$. The empirical distribution of $\{\tau^{(1)}(R_j, S_k), \dots, \tau^{(B)}(R_j, S_k)\}$ represents the posterior distribution of coherence for this cell. We construct a credible interval $[\tau_{\text{low}}, \tau_{\text{high}}]$ from the empirical quantiles and compute the posterior probability of meaningful coherence:

$$P(\tau(R_j, S_k) > \delta \mid \text{data}) \approx \frac{1}{B} \sum_{b=1}^B \mathbb{I}\{\tau^{(b)}(R_j, S_k) > \delta\}, \quad (43)$$

for a scientifically meaningful threshold δ (for example, $\delta = 0.5$ indicating moderate association on average).

This cell-level inference enjoys several advantages over vertex-wise or feature-wise testing. First, by aggregating over vertices in a region and features in a module, we gain statistical power through strength borrowing. If individual features show only moderate associations but ten features in a module all show consistent moderate associations in the same direction, the coherence measure detects this collective signal that individual tests might miss.

Second, the cell structure naturally handles multiple testing: we assess $K \times M$ region-module pairs rather than $n \times m$ vertex-feature pairs, dramatically reducing the multiple comparison burden when $K \ll n$ and $M \ll m$. Third, the inference directly addresses the scientific question of interest: which feature modules associate with outcomes in which sample contexts, providing interpretable summaries for downstream mechanistic investigation.

We can extend the inference to compare coherence across cells. For instance, does module S_1 show stronger association with outcome in region R_1 than in region R_2 ? The posterior distribution over differences $\tau(R_1, S_1) - \tau(R_2, S_1)$ quantifies evidence for region-specific effects. Large positive differences with high posterior probability indicate that the module operates differently across regions, while differences indistinguishable from zero suggest the module-outcome relationship is spatially homogeneous.

6.7 Relationship Between Gradient Flow and Co-Monotonicity Cells

The geometric decomposition framework provides two complementary strategies for partitioning the sample space: gradient flow cells based on outcome landscape geometry (Sections 2–3) and co-monotonicity cells based on association profile clustering (Section 6). These partitions arise from fundamentally different criteria and need not coincide, yet their relationship reveals important insights about the structure of feature-outcome associations.

Gradient flow cells partition vertices based on monotonic behavior of the smoothed outcome \hat{y} . Vertices in the same gradient flow cell lie in a region where \hat{y} varies monotonically from a local minimum to a local maximum, with no intervening extrema. This partition reflects the geometric organization of outcome values in the ambient feature space. In contrast, co-monotonicity cells partition vertices based on similarity of association profiles between outcome and features. Two vertices belong to the same co-monotonicity cell if they have similar co-monotonicity vectors $\widetilde{\text{cm}}(\hat{y}, \hat{Z})$, regardless of their outcome values or position in the gradient flow structure.

When gradient flow and co-monotonicity cells align, the concordance provides strong evidence for a mechanistic interpretation. If gradient flow cell $C(m, M)$ largely overlaps with co-monotonicity region R_j , and if region R_j exhibits strong coherence with feature module S_k , we infer that the features in S_k drive the monotonic outcome variation within cell $C(m, M)$. The outcome increases from minimum m to maximum M because features in module S_k change monotonically along the same gradient paths, and their collective variation explains the outcome behavior. This alignment suggests a causal or mechanistic relationship: the features not only associate with outcomes but do so in a spatially organized manner that respects the geometric structure of the outcome landscape.

Conversely, when gradient flow and co-monotonicity cells disagree, the discordance reveals complexity in the feature-outcome relationships. A single gradient flow cell might span multiple co-monotonicity regions, indicating that different feature modules drive the outcome variation in different parts of the cell. The outcome increases monotonically throughout the cell, but the mechanisms responsible for this increase differ across subregions. Alterna-

tively, a single co-monotonicity region might span multiple gradient flow cells, suggesting that the same feature module associates with outcomes throughout this broader region despite non-monotonic outcome variation within it. Such discordance indicates that association patterns operate at a different spatial scale than outcome gradients, or that multiple compensatory mechanisms produce similar outcomes through different pathways.

The joint analysis of gradient flow and co-monotonicity structures enables more nuanced inference than either approach alone. We can assess whether features in module S_k exhibit different associations within gradient flow cells that intersect co-monotonicity region R_j , testing for context-dependent modulation of associations by outcome level. We can identify features that show strong association throughout a co-monotonicity region spanning multiple gradient cells, suggesting they influence outcomes broadly across different outcome ranges. We can detect regions where outcome gradients are steep but associations weak, indicating that unmeasured features or environmental factors drive the outcome variation.

6.8 Summary

The geometric multiple testing framework via co-monotonicity cells addresses the fundamental challenge of discovering spatially heterogeneous multivariate associations. By embedding vertices into association space through co-monotonicity profiles and applying community detection to the induced graph, we partition both the sample space and feature space simultaneously, identifying regions where specific feature modules exhibit coherent relationships with outcomes. The Bayesian uncertainty quantification through posterior sampling provides credible regions and modules with formal probability interpretations, while the region-module coherence measure enables statistical inference that borrows strength across vertices and features within cells. This approach dramatically reduces the multiple testing burden from $n \times m$ vertex-feature pairs to $K \times M$ region-module coherences where $K \ll n$ and $M \ll m$, while revealing context-dependent association patterns that global methods would obscure and individual tests would lack power to detect. The comparison between gradient flow cells (outcome-driven partitioning) and co-monotonicity cells (association-driven partitioning) provides complementary perspectives on the geometric organization of high-dimensional data, with concordance between partitions suggesting mechanistic coherence and discordance revealing multiple pathways to similar outcomes.

7. Discussion

We have developed a geometric framework for statistical inference on high-dimensional structured data that addresses a fundamental challenge: when features associate with outcomes differently across regions of the sample space, global methods dilute these signals while local methods lack the power and interpretability to discover the underlying structure. Our approach transforms this challenge into a geometric problem, representing data through Riemannian graphs and discovering structure through two complementary decomposition strategies.

7.1 Summary of Contributions

The first strategy employs gradient flow analysis to partition the sample space based on outcome geometry. Given a smoothed estimate of conditional expectation on graph vertices, we compute discrete gradient trajectories through validated gradient flow that addresses the long edge problem via path monotonicity. Long edges connecting geometrically distant points often create artifacts in naive gradient flow computation, with trajectories jumping between basins. Our path monotonicity criterion validates edges by verifying that alternative paths exhibit consistent monotonic behavior, ensuring gradient flow follows the intrinsic data geometry rather than graph construction artifacts. The resulting basins of attraction partition vertices into gradient flow cells where outcomes vary monotonically, providing natural regions for regional statistical modeling.

The second strategy discovers structure through association patterns rather than outcome values. Co-monotonicity coefficients quantify directional concordance between functions at individual graph vertices, measuring whether two functions tend to change together or oppositely across incident edges. These vertex-level measures respect graph geometry through derivative weighting that normalizes by edge length, connecting to angular correlation of gradients in the continuous limit. By computing co-monotonicity between outcomes and features, as well as among features themselves, we construct association profiles that embed vertices into a high-dimensional space where geometric proximity reflects similarity in how features relate to outcomes. Community detection on graphs constructed in this association space induces biclustering, simultaneously partitioning vertices into regions and features into modules. The resulting co-monotonicity cells identify where specific feature combinations drive outcomes, revealing multivariate association structure that univariate methods cannot capture.

For statistical inference, we develop both classical and Bayesian approaches. Vertex-wise permutation testing provides distribution-free inference with exact finite-sample control of type I error rates, employing FDR correction and spatial thresholding to handle multiple comparisons. More fundamentally, we develop Bayesian inference through posterior sampling on weighted Laplacians, using Dirichlet resampling to perturb vertex masses and generate ensembles of smoothed estimates. This propagates uncertainty from estimation through association quantification, yielding credible intervals and posterior probabilities for effect sizes. The Bayesian framework extends naturally to biclustering: computing co-clustering probabilities across posterior samples quantifies uncertainty in the discovered partition structure itself, enabling formal inference on region-module coherences with strength borrowing across vertices and features within cells.

7.2 Implementation and Validation

The methods are implemented in the R package `gflow`, which provides computationally efficient C++ implementations of core algorithms with CRAN-compliant interfaces. Detailed implementation documentation, computational complexity analysis, performance optimization strategies, and comprehensive empirical validation on real datasets will be provided in subsequent versions of this manuscript. The package is designed for production use

in high-dimensional biomarker studies, with particular emphasis on microbiome-outcome association analysis where the methods were originally developed.

7.3 Relationship to Existing Methodologies

Our work builds on and extends several methodological traditions. Morse-Smale regression, introduced by Gerber et al., pioneered the application of discrete Morse theory to statistical regression on graphs. Our contributions advance this framework through robust conditional expectation estimation on density-aware Riemannian graphs (detailed in the companion paper on adaptive geometric regression), systematic treatment of spurious extrema through prominence filtering and basin overlap clustering, path monotonicity validation that resolves long edge artifacts through geometric rather than heuristic criteria, and co-monotonicity measures that provide alternatives to linear models within cells while enabling discovery of association-driven structure complementary to outcome-driven gradient flow decomposition.

The framework situates within geometric data analysis rather than topological data analysis. While TDA emphasizes topological invariants like homology groups and persistence diagrams that remain unchanged under continuous deformations, our approach focuses on geometric properties like distances, angles, and geodesics that depend on specific metric structure. The Riemannian graphs with vertex and edge masses capture local density and geometry that spectral methods exploit for inference. The gradient flow respects this geometry through path monotonicity validation and through the Riemannian metric implicit in the normalized Laplacian. This geometric emphasis connects our work to manifold learning and spectral graph theory more than to persistent homology, though we acknowledge that the basin complex structure has topological aspects.

From a statistical perspective, our geometric decomposition provides data-driven stratification for inference. Stratified sampling and testing are well-established in statistics, typically requiring investigators to specify strata based on known covariates. Our contribution makes stratification itself a geometric inference problem: strata emerge from graph structure through gradient flow or co-monotonicity analysis rather than being predetermined. This connects to recent work on conditional independence testing and context-specific associations, but grounds these ideas in explicit geometric partitions of the sample space derived from the Riemannian structure.

Compared to standard correlation-based methods, co-monotonicity offers several advantages. Classical correlation measures linear association globally, treating all observations as equally related and summarizing with a single coefficient. Co-monotonicity provides spatially-resolved assessment of directional concordance, detecting where associations are strong or weak across the graph while accounting for edge geometry through derivative weighting. This local perspective reveals regional heterogeneity that global methods obscure. Moreover, the augmented co-monotonicity embedding incorporating inter-feature associations enables discovery of feature modules with coherent relationships, information that pairwise correlations between outcome and individual features cannot capture.

7.4 Limitations and Future Directions

Several limitations suggest directions for future development. The k -nearest neighbor graph construction introduces discrete approximation of the underlying manifold, with performance sensitive to the neighborhood size parameter k . While we employ principled selection based on connectivity and local geometry, the optimal k remains data-dependent. Adaptive graph construction methods that locally vary neighborhood size or employ data-dependent distance metrics may improve approximation quality.

The current framework applies to continuous or binary outcomes through spectral filtering on the graph Laplacian. Extension to general discrete outcomes (count data, categorical responses) and survival outcomes (time-to-event data) requires development of appropriate smoothing operators that respect the outcome type while preserving the geometric structure. Preliminary work on Poisson regression suggests that weighted Laplacians with outcome-dependent masses can accommodate count responses, but comprehensive treatment awaits future investigation.

Computational scaling presents challenges for very high-dimensional feature spaces. Computing the augmented co-monotonicity embedding requires $O(m^2)$ coefficients for m features, and the induced graph $G_k(\text{cm})$ in dimension $m(m+1)/2$ may suffer from curse of dimensionality when m is large. Dimensionality reduction through principal component analysis on association profiles, or projection pursuit methods that identify discriminating directions in association space, may alleviate this burden. Alternatively, sparse formulations that compute only selected inter-feature associations could reduce dimensionality while preserving essential structure.

The path monotonicity validation criterion for long edges employs heuristic thresholds (quantile $q \in [0.75, 0.90]$ for identifying long edges, threshold $\theta \in [0.85, 0.95]$ for accepting monotonicity). While these ranges perform well empirically across diverse datasets in our experience, principled data-driven selection of these parameters through cross-validation or information criteria would strengthen the methodology. Theoretical analysis characterizing the relationship between threshold choice and basin structure properties could guide selection.

Several promising extensions warrant exploration. The framework naturally accommodates multi-modal data integration: constructing co-monotonicity embeddings that incorporate associations within and between multiple feature sets (genomic, proteomic, metabolomic) enables joint analysis that leverages complementary information. Temporal extensions for longitudinal data could track how co-monotonicity cells evolve over time, identifying feature modules whose relationships with outcomes change with disease progression or treatment. Causal inference extensions employing directed graphs and structural equation models could move beyond association to intervention prediction, answering questions about which features to manipulate to alter outcomes.

7.5 Broader Impact

The geometric framework addresses methodological challenges that appear across scientific domains wherever high-dimensional structured data and context-dependent relation-

ships arise. In microbiome research, the methods enable discovery of microbial community structures that associate with health outcomes, revealing that the same bacterial taxa may promote or protect against disease depending on the broader community context. In single-cell genomics, gradient flow cells could identify cell state trajectories while co-monotonicity cells discover gene modules with coordinated expression programs that vary across cell types. In spatial transcriptomics, the framework can partition tissue regions based on molecular signatures and identify context-dependent gene-phenotype relationships across anatomical structures. In ecological data, co-monotonicity analysis could reveal how species interactions vary across environmental gradients, with different competitive or mutualistic networks operating in different habitats.

Beyond specific applications, the framework demonstrates the value of geometry-first approaches to statistical inference on complex data. Rather than treating samples as unstructured collections of observations, we represent them through graphs that encode proximity relationships, equip these graphs with Riemannian structure that respects local density and geometry, and discover structure through gradient flow and association profiles that respect this geometry. This perspective bridges differential geometry, spectral graph theory, and statistical inference, providing a mathematically principled foundation for methods that adapt to intrinsic data structure rather than imposing ambient Euclidean geometry.

The Bayesian inference framework we develop addresses a conceptual limitation of classical hypothesis testing that becomes acute in exploratory high-dimensional analysis. Traditional p -values answer the question "how surprising would the data be if no association existed?" but investigators typically care more about "how strong is the evidence for meaningful association?" and "how uncertain are we about effect magnitudes?" Posterior probabilities and credible intervals directly address these questions, enabling principled uncertainty quantification that propagates through the entire analysis pipeline from conditional expectation estimation through biclustering to cell-level coherence assessment. This approach aligns with growing recognition in statistics that effect sizes and uncertainty bounds provide more actionable information than binary significance decisions.

7.6 Conclusion

We have developed a comprehensive geometric framework for discovering and quantifying spatially heterogeneous associations in high-dimensional structured data. By representing samples through Riemannian graphs, employing path-validated gradient flow to partition based on outcome geometry, defining co-monotonicity coefficients that respect graph structure, and constructing association space embeddings that enable biclustering, the framework addresses limitations of global methods that assume homogeneous relationships and local methods that lack power to detect structure. The Bayesian posterior sampling approach provides rigorous uncertainty quantification that respects the geometry of the data manifold while enabling inference at multiple scales, from individual vertices to regional coherence measures.

The framework extends naturally to multi-modal data integration, temporal dynamics, and potentially causal inference, suggesting a broad research program for geometric statistical inference. While substantial work remains in implementation optimization, theoretic

cal convergence analysis, and empirical validation across diverse application domains, the core methodological contributions presented here provide a foundation for this program. Detailed computational documentation, formal theoretical results, and comprehensive real-data case studies will be provided in subsequent versions of this manuscript.

The methods are implemented in the R package `gflow`, available at <https://github.com/pgajer/gflow>, enabling immediate application by researchers facing similar challenges in their own high-dimensional biomarker studies. We anticipate that the geometric perspective on association analysis will prove valuable across scientific domains where understanding context-dependent relationships is essential for mechanistic insight and intervention design.

References

- [1] Manimozhiyan Arumugam, Jeroen Raes, Eric Pelletier, Denis Le Paslier, Takuji Yamada, Daniel R. Mende, Gabriel R. Fernandes, Julien Tap, Thomas Bruls, Jean-Michel Batto, Marcelo Bertalan, Natalia Borruel, Francesc Casellas, Leyden Fernandez, Laurent Gautier, Torben Hansen, Masahira Hattori, Tetsuya Hayashi, Michiel Kleerebezem, Ken Kurokawa, Marion Leclerc, Florence Levenez, Chaysavanh Manichanh, H. Bjørn Nielsen, Trine Nielsen, Nicolas Pons, Julie Poulain, Junjie Qin, Thomas Sicheritz-Ponten, Sebastian Tims, David Torrents, Edgardo Ugarte, Erwin G. Zoetendal, Jun Wang, Francisco Guarner, Oluf Pedersen, Willem M. de Vos, Søren Brunak, Joël Doré, and MetaHIT Consortium. Enterotypes of the human gut microbiome. *Nature*, 473(7346):174–180, 2011.
- [2] Mikhail Belkin, Partha Niyogi, and Vikas Sindhwani. Manifold regularization: A geometric framework for learning from labeled and unlabeled examples. *Journal of Machine Learning Research*, 7:2399–2434, 2006.
- [3] Richard Bellman. *Adaptive Control Processes: A Guided Tour*. Princeton University Press, Princeton, New Jersey, 1961.
- [4] Emelie Berglund, Jonas Maaskola, Niklas Schultz, Stefanie Friedrich, Maja Marklund, Joseph Bergenstråhle, Firas Tarish, Anna Tanoglidi, Sanja Vickovic, Ludvig Larsson, et al. Spatial maps of prostate cancer transcriptomes reveal an unexplored landscape of heterogeneity. *Nature communications*, 9(1):2419, 2018.
- [5] Gunnar Carlsson. Topology and data. *Bulletin of the American Mathematical Society*, 46(2):255–308, 2009.
- [6] Fan RK Chung and F Chung Graham. *Spectral graph theory*. Number 92 in CBMS Regional Conference Series in Mathematics. American Mathematical Society, 1997.
- [7] William G Cochran. *Sampling techniques*. John Wiley & Sons, New York, 3 edition, 1977.
- [8] Ronald R Coifman and Stéphane Lafon. Diffusion maps. *Applied and computational harmonic analysis*, 21(1):5–30, 2006.

- [9] Inderjit S Dhillon. Co-clustering documents and words using bipartite spectral graph partitioning. In *Proceedings of the seventh ACM SIGKDD international conference on Knowledge discovery and data mining*, pages 269–274, 2001.
- [10] Herbert Edelsbrunner and John L Harer. *Computational topology: an introduction*. American Mathematical Society, 2022.
- [11] Michal A Elovitz, Pawel Gajer, Virginia Riis, Amy G Brown, Michael S Humphrys, Johanna B Holm, and Jacques Ravel. Cervicovaginal microbiota and local immune response modulate the risk of spontaneous preterm delivery. *Nature Communications*, 10(1):1305, 2019.
- [12] Jianqing Fan and Jinchi Lv. A selective overview of variable selection in high dimensional feature space. *Statistica Sinica*, 20(1):101, 2010.
- [13] Charles Fefferman, Sanjoy Mitter, and Hariharan Narayanan. Testing the manifold hypothesis. *Journal of the American Mathematical Society*, 29:983–1049, 2016.
- [14] Jennifer M Fettweis, Myrna G Serrano, J Paul Brooks, David J Edwards, Philippe H Girerd, Hardik I Parikh, Bernice Huang, Tomasz J Arodz, Lavanya Edupuganti, Abigail L Glascock, et al. The vaginal microbiome and preterm birth. *Nature Medicine*, 25(6):1012–1021, 2019.
- [15] Pawel Gajer and Jacques Ravel. Adaptive geometric regression for high-dimensional structured data. *arXiv preprint*, 2025. Submitted November 5, 2025.
- [16] Samuel Gerber, Oliver Rübél, Peer-Timo Bremer, Valerio Pascucci, and Ross T Whitaker. Morse–smale regression. *Journal of Computational and Graphical Statistics*, 22(1):193–214, 2013.
- [17] Peter D. Hoff, Adrian E. Raftery, and Mark S. Handcock. Latent space approaches to social network analysis. *Journal of the American Statistical Association*, 97(460):1090–1098, 2002.
- [18] Yuval Kluger, Ronen Basri, Joseph T Chang, and Mark Gerstein. Spectral biclustering of microarray data: coclustering genes and conditions. *Genome Research*, 13(4):703–716, 2003.
- [19] Owen R Liu and Steven D Gaines. Environmental context dependency in species interactions. *Proceedings of the National Academy of Sciences*, 119(36):e2118539119, 2022.
- [20] László Lovász. Random walks on graphs: A survey. In *Combinatorics, Paul Erdős is Eighty*, volume 2, pages 1–46. János Bolyai Mathematical Society, Budapest, 1993.
- [21] Marston Morse. *The Calculus of Variations in the Large*, volume 18 of *Colloquium Publications*. American Mathematical Society, Providence, RI, 1934.

- [22] Jacques Ravel, Pawel Gajer, Zaid Abdo, G. Maria Schneider, Sara S. K. Koenig, Stacey L. McCulle, Shara Karlebach, Reshma Gorle, Jennifer Russell, Carol O. Tacket, Rebecca M. Brotman, Catherine C. Davis, Kevin Ault, Ligia Peralta, and Larry J. Forney. Vaginal microbiome of reproductive-age women. *Proceedings of the National Academy of Sciences*, 108(Supplement 1):4680–4687, 2011.
- [23] Sam T. Roweis and Lawrence K. Saul. Nonlinear dimensionality reduction by locally linear embedding. *Science*, 290(5500):2323–2326, 2000.
- [24] Rajen D Shah and Jonas Peters. The hardness of conditional independence testing and the generalised covariance measure. *The Annals of Statistics*, 48(3):1514–1538, 2020.
- [25] Alexander J. Smola and Risi Kondor. Kernels and regularization on graphs. In Bernhard Schölkopf and Manfred K. Warmuth, editors, *Learning Theory and Kernel Machines: 16th Annual Conference on Learning Theory and 7th Kernel Workshop, COLT/Kernel 2003*, volume 2777 of *Lecture Notes in Computer Science*, pages 144–158, Berlin, Heidelberg, 2003. Springer.
- [26] Joshua B. Tenenbaum, Vin de Silva, and John C. Langford. A global geometric framework for nonlinear dimensionality reduction. *Science*, 290(5500):2319–2323, 2000.
- [27] Robert Tibshirani. Regression shrinkage and selection via the lasso. *Journal of the Royal Statistical Society Series B: Statistical Methodology*, 58(1):267–288, 1996.
- [28] Cole Trapnell. Defining cell types and states with single-cell genomics. *Genome Research*, 25(10):1491–1498, 2015.
- [29] Cole Trapnell, Davide Cacchiarelli, Jonna Grimsby, Prapti Pokharel, Shuqiang Li, Michael Morse, Niall J. Lennon, Kenneth J. Livak, Tarjei S. Mikkelsen, and John L. Rinn. The dynamics and regulators of cell fate decisions are revealed by pseudotemporal ordering of single cells. *Nature Biotechnology*, 32(4):381–386, 2014.
- [30] Edward Witten. Supersymmetry and morse theory. *Journal of Differential Geometry*, 17(4):661–692, 1982.
- [31] Hui Zou and Trevor Hastie. Regularization and variable selection via the elastic net. *Journal of the Royal Statistical Society: Series B*, 67(2):301–320, 2005.